

DEPENDENCE OF GALACTIC HALO KINEMATICS ON THE ADOPTED GALACTIC POTENTIAL

YOUNG KWANG KIM¹, YOUNG SUN LEE^{1,3}, AND TIMOTHY C. BEERS²

Draft version, June 13, 2019

ABSTRACT

We explore differences in Galactic halo kinematic properties derived from two commonly employed Galactic potentials: the Stäckel potential and the default Milky Way-like potential used in the “Galpy” package (MWPotential2014), making use of stars with available metallicities, radial velocities, and proper motions from Sloan Digital Sky Survey Data Release 12. Adopting the Stäckel potential, we find that the shape of the metallicity distribution function (MDF) and the distribution of orbital rotation abruptly change at $Z_{\max} = 15$ kpc and $r_{\max} = 30$ kpc (where Z_{\max} and r_{\max} are the maximum distances reached by a stellar orbit from the Galactic plane and from the Galactic center, respectively), indicating that the transition from dominance by the inner-halo stellar population to the outer-halo population occurs at those distances. Stars with $Z_{\max} > 15$ kpc show an average retrograde motion of $V_{\phi} = -60$ km s⁻¹, while stars with $r_{\max} > 30$ kpc exhibit an even larger retrograde value, $V_{\phi} = -150$ km s⁻¹. This retrograde signal is also confirmed using the sample of stars with radial velocities obtained by *Gaia* Data Release 2, assuming the Stäckel potential. In comparison, when using the shallower Galpy potential, a noticeable change in the MDF occurs only at $Z_{\max} = 25$ kpc, and a much less extreme retrograde motion is derived. This difference arises because stars with highly retrograde motions in the Stäckel potential are unbound in the shallower Galpy potential, and stars with lower rotation velocities reach larger Z_{\max} and r_{\max} . The different kinematic characteristics derived from the two potentials suggest that the nature of the adopted Galactic potential can strongly influence interpretation of the properties of the Galactic halo.

Keywords: Galaxy: halo — methods: data analysis — stars: kinematics and dynamics

1. INTRODUCTION

Although comprising only about 1% of the Galaxy’s total stellar mass, the stellar halo of the Milky Way (MW) provides valuable clues to its formation and evolutionary history. Recent studies (e.g., Yanny et al. 2000; Newberg et al. 2002; Majewski et al. 2003; Belokurov et al. 2006; Bonaca et al. 2012) from large-scale sky surveys such as the Sloan Digital Sky Survey (SDSS; York et al. 2000) have shown that the MW’s halo includes multiple stellar components and continually accretes stars from dwarf galaxies disrupted by the MW’s tidal forces. Thanks to the long dynamical timescale for accreted stars to be completely mixed into the halo, the Galactic halo serves as a fossil record, revealing its accretion history (Bland-Hawthorn & Gerhard 2016).

The Λ -cold dark matter (Λ -CDM) scenario predicts that large galaxies, such as the MW, formed via hierarchical mergers (White & Frenk 1991). The majority of the halo is built at early times, with most of the halo stars coming from the mergers of a few massive satellites (Bullock & Johnston 2005). According to more sophisticated simulations of galaxy formation, the halos of galaxies like the MW have a dual origin, and the inner and outer regions of their halos might be dominated by accreted stellar populations with different chemical and kinematic properties, respectively (Abadi et al. 2006; Zolotov et al. 2009; Font et al. 2011; McCarthy et al. 2012; Tissera et al. 2012, 2013, 2014; Cooper et al. 2015).

From a kinematic analysis of halo stars within 4 kpc of the Sun, Carollo et al. (2007) first argued that the Galactic halo is composed of at least two distinct stellar populations — an inner-halo population (IHP) and an outer-halo population (OHP), separable by their different spatial distribution, metallicity, and kinematics. The inner-halo component dominates the population of stars found at distances up to 10 – 15 kpc from the Galactic center, while the outer-halo component is dominant in the region beyond 15 – 20 kpc. The inner halo also exhibits a flatter density profile than the nearly spherical outer halo. The metallicity distribution function (MDF) of the inner-halo stars peaks at $[\text{Fe}/\text{H}] = -1.6$, while the peak of the MDF for the outer-halo stars occurs at $[\text{Fe}/\text{H}] = -2.2$. Kinematically, the IHP shows either zero or slightly prograde rotation and eccentric orbits, while the OHP exhibits a net retrograde rotation of about -80 km s⁻¹ on more circular (or less eccentric) orbits (Carollo et al. 2007, 2010; Beers et al. 2012).

However, Schönrich et al. (2011, 2014) claimed that the results by Carollo et al. (2010) might have arisen due to faulty distance determinations and unaccounted-for selection biases; their reanalysis of the data used by Carollo et al. (2010) does not support the claim of retrograde motion for the OHP. Schönrich et al. (2014) further argued that the results of Carollo et al. (2007, 2010) needed to account for a possible metallicity bias in their selection and verify whether or not the claimed retrograde motion is due to observational errors. In the meantime, Beers et al. (2012) disputed these arguments and reported that the result of Schönrich et al. (2011) is due, at least in part, to their adoption of an incorrect main-sequence absolute-magnitude relationship. Furthermore,

¹ Department of Astronomy and Space Science, Chungnam National University, Daejeon 34134, Republic of Korea

² Department of Physics and JINA Center for the Evolution of the Elements, University of Notre Dame, IN 46556, USA

³ Corresponding author; youngsun@cnu.ac.kr

they demonstrated that the retrograde signature of the OHP appears using proper motions alone. This interpretation is also supported by a recent study (Tian et al. 2019) of local K-giant stars selected from the Large Sky Area Multi-Object Fiber Spectroscopic Telescope (LAMOST; Cui et al. 2012). In addition, many recent studies of in situ halo stars up to tens of kpc away from the Galactic center consistently support the dual nature of the Galactic halo (e.g., de Jong et al. 2010; Deason et al. 2011; An et al. 2013, 2015; Kafle et al. 2013, 2017; Allende Prieto et al. 2014; Chen et al. 2014; Fernandez-Alvar et al. 2015; Das & Binney 2016).

For in situ studies of the most distant halo kinematics, one can only rely on radial-velocity information (e.g., Deason et al. 2011; Kafle et al. 2013, 2017). However, it is feasible to consider the full six-dimensional location and velocity phase space of halo stars reaching large Galactocentric distance derived from stars in the Solar neighborhood, where proper motions can be readily measured. In this case, however, a Galactic gravitational potential must be adopted in order to compute stellar orbital parameters, such as eccentricity, apo-Galacticon and peri-Galacticon distances, and maximum distance from the Galactic midplane, which are used to separate the stellar populations in the Galactic halo system. Even though it is recognized that the adoption of different potentials (and masses) can influence the interpretation of the chemical and kinematic properties of the halo, to date there has not been *quantitative* investigation of these effects. This is the key motivation for pursuing the present study.

In this paper, we consider two well-known and often-adopted Galactic potentials—a Stäckel-type potential (hereafter referred to as “the Stäckel potential”) employed by Chiba & Beers (2000) and Carollo et al. (2007, 2010), and the MWPotential2014 (hereafter referred to as “the Galpy potential”) included in the Galpy package by Bovy (2015)—and examine the resulting influence on the derived chemical and kinematic properties, as well as the corresponding interpretation of the nature of the MW halo system.

The major difference between the two potentials is the assumed total mass of the MW. The total mass adopted in the Stäckel potential exceeds that of the Galpy potential; hence the Stäckel potential well is deeper than that of the Galpy potential. This results in larger numbers of stars inferred to be bound (total energy (TE) < 0) to the Galaxy in the Stäckel potential compared with the Galpy potential. Accordingly, derived apo-Galacticon distances and maximum distances from the Galactic midplane for commonly bound stars in both potentials are larger in the Galpy potential than in the Stäckel potential.

This paper is outlined as follows. We describe the criteria used to select a local sample for our study in Section 2. Section 3 addresses the derivation of velocity components and orbital parameters for the stars in our sample. In Section 4, we compare the chemical and kinematic properties of the Galactic halo based on orbital parameters derived from both potentials. We examine the impact of distance errors and target selection effects on the chemical and kinematic properties of the Galactic halo in Section 5. Section 6 discusses our findings on the nature of the Galactic halo, and a summary follows in Section 7.

2. SELECTION OF LOCAL SAMPLE STARS

The sample used in this study consists of spectrophotometric and telluric calibration stars observed during the course of the legacy SDSS and Sloan Extension for Galactic Exploration and Understanding (SEGUE; Yanny et al. 2009) as well as the Baryon Oscillation Spectroscopic Survey (BOSS; Dawson et al. 2013). The apparent magnitude and color ranges of the calibration stars are $15.5 < g_0 < 18.5$, and $0.6 < (u - g)_0 < 1.2$ and $0.0 < (g - r)_0 < 0.6$, after correcting for the effects of interstellar absorption and reddening based on the dust map of Schlegel et al. (1998). The calibration stars are assembled from the SDSS Data Release 12 (SDSS DR12; Alam et al. 2015); the total number of stars is 55,293.

Stellar atmospheric parameters (T_{eff} , $\log g$, and $[\text{Fe}/\text{H}]$) for the calibration stars were estimated using the SEGUE Stellar Parameter Pipeline (SSPP; Allende Prieto et al. 2008; Lee et al. 2008a,b, 2011; Smolinski et al. 2011) from the medium-resolution ($R \sim 2000$) SDSS spectra. Radial velocities were adopted from the SDSS pipeline; they have precisions of 5–20 km s^{−1}, depending on the signal-to-noise ratio (S/N) of the spectrum, and negligible zero-point errors (Yanny et al. 2009). For stellar distance estimates, we employed the methods of Beers et al. (2000, 2012); the reported uncertainty is on the order of 15–20%. Proper motions, which are corrected for known systematic errors, were obtained from the SDSS DR12 (Munn et al. 2004, 2008). Even though the proper motions from the *Gaia* Data Release 2 (*Gaia* DR2; Gaia Collaboration et al. 2018) are now available, we used the proper motions from the SDSS DR12 in order to enable a more direct comparison with previous studies (e.g., Carollo et al. 2010). We adopted the criteria used by Carollo et al. (2010) to select the final sample for our analysis. Those criteria are as follows:

- The spectra must have an average S/N greater than 10/1, as well as effective temperatures in the range $4500 \leq T_{\text{eff}} \leq 7000$ K.
- Stars must have a measured radial velocity with reported error better than 20 km s^{−1}, as well as proper motions with errors less than 4 mas yr^{−1} (or relative proper motion errors less than 10%).
- Stars must have distances of $d < 4$ kpc from the Sun.
- Stars must reside in the distance range of $6 < R < 10$ kpc from the Galactic center, projected onto the Galactic plane.

In our study, we considered two samples. The first sample, which we refer to as the “DR7 sample,” consists of 18,821 calibration stars of the SDSS Data Release 7 (SDSS DR7; Abazajian et al. 2009), subselected from the SDSS DR12. This is the same sample used by Carollo et al. (2010). The other one is an extended sample of 29,447 calibration stars from the SDSS DR12, which we refer to as the “DR12 sample.” The DR12 sample also includes stars from the DR7 sample. The reason for using the same sample as Carollo et al. is that we want to check whether we are able to derive the same Galactic halo properties from an application of a different Galactic

potential. The much larger DR12 sample is used to check whether we obtain evidence for the dual nature of the Galactic halo from the two different Galactic potentials considered.

3. CALCULATIONS OF SPACE VELOCITY COMPONENTS AND ORBITAL PARAMETERS

Based on the distances, radial velocities, and proper motions adopted for our sample of stars, we derived their space velocity components in a spherical coordinate system, after correcting for the solar motion. We adopted $V_{\text{LSR}} = 220 \text{ km s}^{-1}$ for the rotation motion of the local standard of rest (LSR) and the Sun's position of $R_{\odot} = 8 \text{ kpc}$ from the Galactic center (note that [Carollo et al. \(2010\)](#) used 8.5 kpc). For the solar peculiar motion with respect to the LSR, we assumed $(U, V, W)_{\odot} = (-10.1, 4.0, 6.7) \text{ km s}^{-1}$ ([Hogg et al. 2005](#)), where the velocity components U , V , and W are positive in the direction toward the Galactic anticenter, Galactic rotation, and north Galactic pole, respectively. In our adopted system, a disk star has a prograde rotation of $V_{\phi} = 220 \text{ km s}^{-1}$ ([Kerr & Lynden-Bell 1986](#)); the retrograde rotation is indicated by $V_{\phi} < 0 \text{ km s}^{-1}$. Stars with $V_r > 0 \text{ km s}^{-1}$ move away from the Galactic center, and stars with $V_{\theta} > 0 \text{ km s}^{-1}$ move toward the south Galactic pole. We also define the tangential velocity, $V_t = \sqrt{V_{\theta}^2 + V_{\phi}^2}$, and the angular momentum, $|\vec{L}| = rV_t$, where r is the distance from the Galactic center to a given star.

We also make use of a Galactocentric Cartesian reference frame denoted by (X, Y, Z) , where the axes are positive in orientation toward the Sun, Galactic rotation, and north Galactic pole, respectively. We introduce an angle (α) between the orientation of the angular momentum vector and the negative Z axis, defined by:

$$\begin{aligned} \alpha &= \cos^{-1} \left(\frac{l_Z}{|\vec{L}|} \right) = \cos^{-1} \left(\frac{rV_{\phi}}{rV_t} \right) \\ &= \cos^{-1} \left\{ \left(\frac{R}{r} \right) \frac{\left(\frac{V_{\phi}}{|V_{\phi}|} \right)}{\sqrt{1 + \left(\frac{V_{\theta}}{|V_{\phi}|} \right)^2}} \right\}, \end{aligned}$$

where l_Z is the Z component of the angular momentum and positive in the negative Z -axis direction. In this notation, stars with $l_Z > 0$ or $V_{\phi} > 0$ have prograde orbits and $\alpha < 90^\circ$. Retrograde orbits have $\alpha > 90^\circ$ and the inclination (i) of their orbital plane increases as α approaches 90° . For prograde motions, the inclination angle $i = \alpha$; for retrograde orbits, $i = 180^\circ - \alpha$.

We used both the Stäckel and the Galpy gravitational potentials to calculate the orbital parameters of our program stars. The Stäckel potential is analytic, consisting of a flattened, oblate disk and a nearly spherical massive dark matter halo. The tidal cutoff radius is 200 kpc, and the disk mass is $M_d = 9.0 \times 10^{10} M_{\odot}$. The central density and mass of the halo are $\rho_0 = 2.45 \times 10^7 M_{\odot} \text{ kpc}^{-3}$ and $M_h (r < 200 \text{ kpc}) = 2.2 \times 10^{12} M_{\odot}$, respectively ([de Zeeuw et al. 1986](#); [Dejonghe & de Zeeuw 1988](#); [Sommer-Larsen & Zhen 1990](#); [Chiba & Beers 2000](#)).

The Galpy potential comprises three components. The bulge is parameterized as a power-law density profile that is exponentially cut off at 1.9 kpc with a power-law ex-

ponent of -1.8 . The disk is represented by a Miyamoto–Nagai potential with a radial scale length of 3 kpc and a vertical scale height 280 pc. The halo is modeled as a Navarro–Frenk–White halo with a scale length of 16 kpc. The bulge and disk masses of the Galpy potential are $M_b = 0.5 \times 10^{10} M_{\odot}$ and $M_d = 6.8 \times 10^{10} M_{\odot}$, respectively. The virial mass of the Galpy potential is $M_{\text{vir}} = 0.8 \times 10^{12} M_{\odot}$ ([Bovy 2015](#)).

The orbital parameters of our sample of stars (for each potential), such as the perigalactic distance (r_{min} , the minimum distance of an orbit from the Galactic center), and the apogalactic distance (r_{max} , the maximum distance of an orbit from the Galactic center) as well as Z_{max} (the maximum distance of a stellar orbit above or below the Galactic plane), are derived from an analytic solution for the Stäckel potential (see the equations of motion in [Sommer-Larsen & Zhen \(1990\)](#)), and integrating their orbital paths for a time of 11 Gyr using the Galpy package ([Bovy 2015](#)) for the Galpy potential, based on the starting position and observed velocities. We describe the method for estimating the uncertainties in the derived parameters in Section 5.1.

These orbital calculations allowed us to obtain, for the DR7 sample orbital parameter, estimates for a total number of $N = 18,749$ and 18,370 stars for the Stäckel and Galpy potentials, respectively. If a star is unbound in the Stäckel potential, we eliminated it from further consideration, so by definition all stars in this potential are bound. The shallower Galpy potential has additional numbers of unbound stars. The total number of stars for the DR12 sample with orbital parameter estimates is 29,273 for the Stäckel potential and 28,483 for the Galpy potential. Note that when we mention unbound stars throughout the rest of the paper, we always mean those that are unbound under the Galpy potential.

4. RESULTS

For simplicity, we focus on the distributions of rotation velocity (V_{ϕ}) and the MDF for comparison of the derived halo properties for the two potentials in our analysis. This also allows for a straightforward comparison with previous studies based on local samples of halo stars, as described below.

4.1. Differences in Halo Properties from the DR7 Sample

In order to compare the derived halo properties between the Stäckel and Galpy potential, we examined the distribution of TE as a function of α , as shown in Figure 1. As described in the previous section, α is the angle between the angular momentum vector and the direction of the negative Z -axis.

The left- and right-column panels in the figure show the stars in the Z_{max} bin listed in the right-column panels, based on the Stäckel and the Galpy potential, respectively. The gray (top panels) and black (bottom panels) maps exhibit the logarithmic number density (low to high from bright to dark) for all bound stars and stars in the range $Z_{\text{max}} < 5 \text{ kpc}$, respectively. In the left column of panels, stars with different colors represent objects in respective Z_{max} cuts from the Stäckel potential. Stars in purple are bound in the Stäckel potential, but unbound in the Galpy potential. In the middle three rows of panels, stars in black with $Z_{\text{max}} < 5 \text{ kpc}$ in the Stäckel

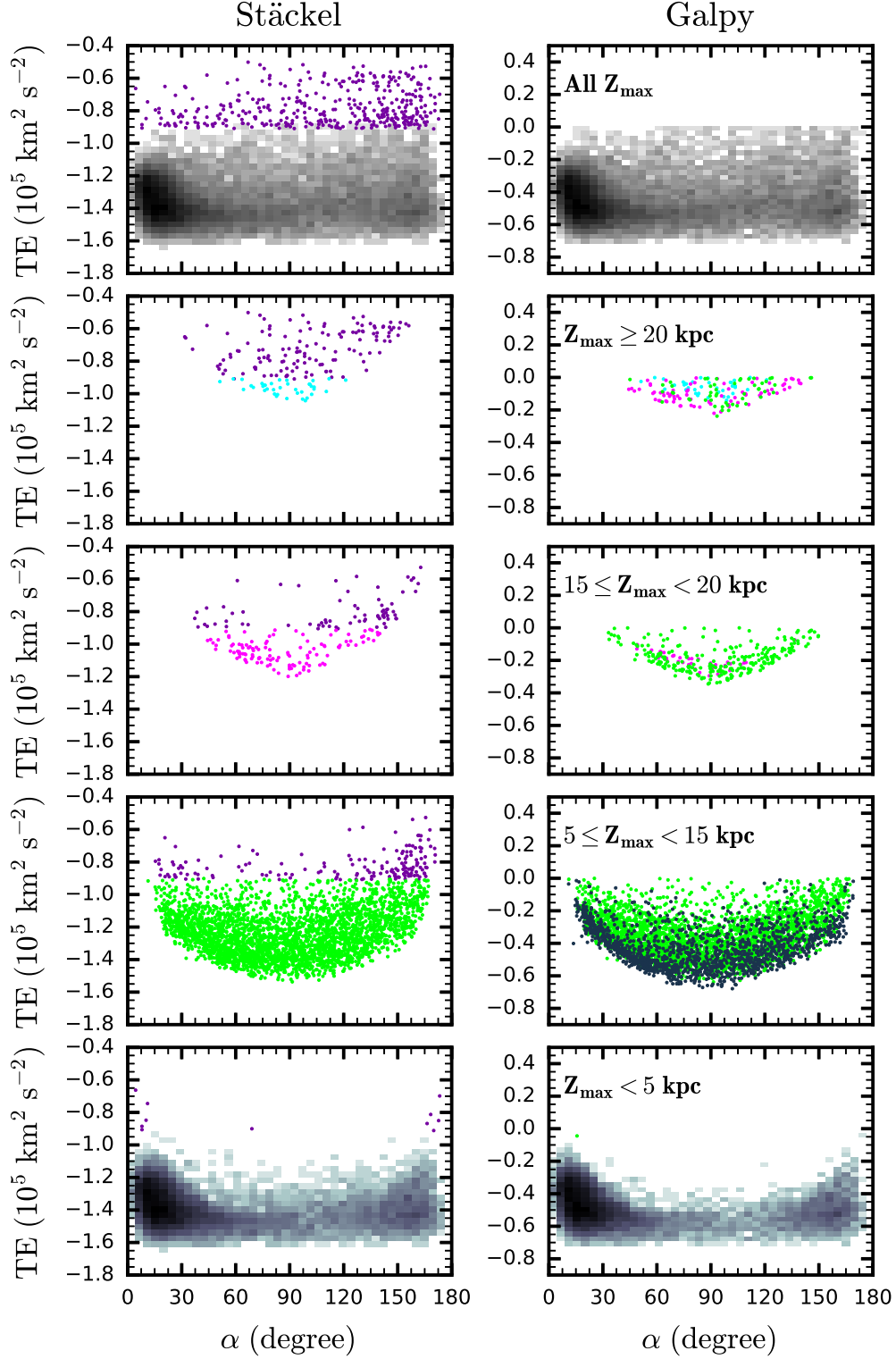


Figure 1. Distribution of total energy (TE) versus α for the Stäckel (left panels) and the Galpy (right panels) potentials, respectively. Note that the scale of the total energy differs between the two potentials in different ranges of Z_{\max} , as listed in the right panels. Here, α is the angle between the direction of the angular momentum vector and the negative Z -axis for each star. Maps in the top and bottom panels display the number density (low to high from bright to dark) on a log-10 based scale for all bound stars and stars with $Z_{\max} < 5$ kpc, respectively. In the left panels, stars in different colors represent objects in respective Z_{\max} cuts from the Stäckel potential. Stars in purple are bound objects in the Stäckel potential, but unbound objects in the Galpy potential. The right panels also show the stars in respective Z_{\max} cuts from the Galpy. The green points from the first to the fourth from the bottom in the right column of panels are for stars in the range of $5 \leq Z_{\max} < 15$ kpc in the Stäckel potential. The black dots in the second panel from the bottom are the stars with $Z_{\max} < 5$ kpc in the Stäckel potential. Similarly, the magenta stars in the right panels are in the range of $15 \leq Z_{\max} < 20$ kpc in the Stäckel potential, while the cyan stars in the right panels are in the range of $Z_{\max} \geq 20$ kpc in the Stäckel potential.

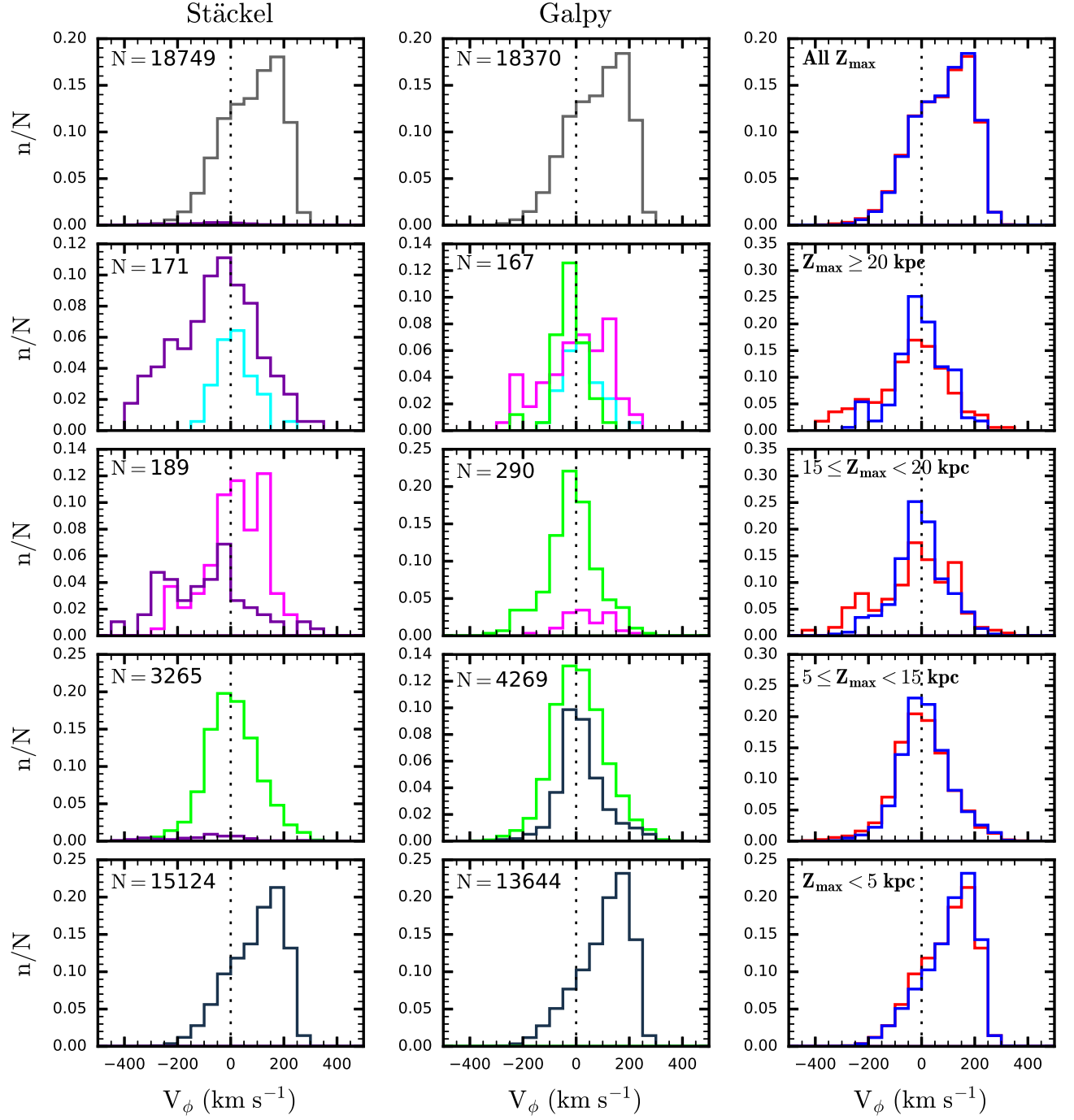


Figure 2. Fractional distribution of the rotation velocities in different bins of Z_{\max} , as listed in the right panels, for the Stäckel (left panels) and the Galpy (middle panels) potentials. Here, N is the total number of stars in each bin. The definition for each color is the same as in Figure 1. The right-column panels display the distribution of rotation velocity for all bound stars in given bin of Z_{\max} for the Stäckel potential as red lines, and for the Galpy potential as blue lines.

potential fall in the ranges $Z_{\max} < 5$ kpc and $5 \leq Z_{\max} < 15$ kpc in the Galpy potential, while stars in green with $5 \leq Z_{\max} < 15$ kpc of the Stäckel potential are located in all Z_{\max} cuts of the Galpy potential. Stars in magenta with $15 \leq Z_{\max} < 20$ kpc in the Stäckel potential occupy the ranges of $15 \leq Z_{\max} < 20$ kpc and $Z_{\max} \geq 20$ kpc of the Galpy potential. Stars with cyan colors with $Z_{\max} \geq 20$ kpc in the Stäckel potential fall in the range $Z_{\max} \geq 20$ kpc in the Galpy potential as well.

Inspection of Figure 1 reveals the following. As Z_{\max} increases, most of the stars tend to cluster around $\alpha = 90^\circ$. For a given interval of Z_{\max} , the stars that are closer to $\alpha = 90^\circ$ have the lowest TE, while the stars progressively farther from $\alpha = 90^\circ$ have larger TE. Considering only the bound stars from each potential, the stars with $Z_{\max} > 5$ kpc show a rather symmetric distribution with respect to $\alpha = 90^\circ$. The green stars reaching high Z_{\max} in the shallower Galpy potential have lower Z_{\max}

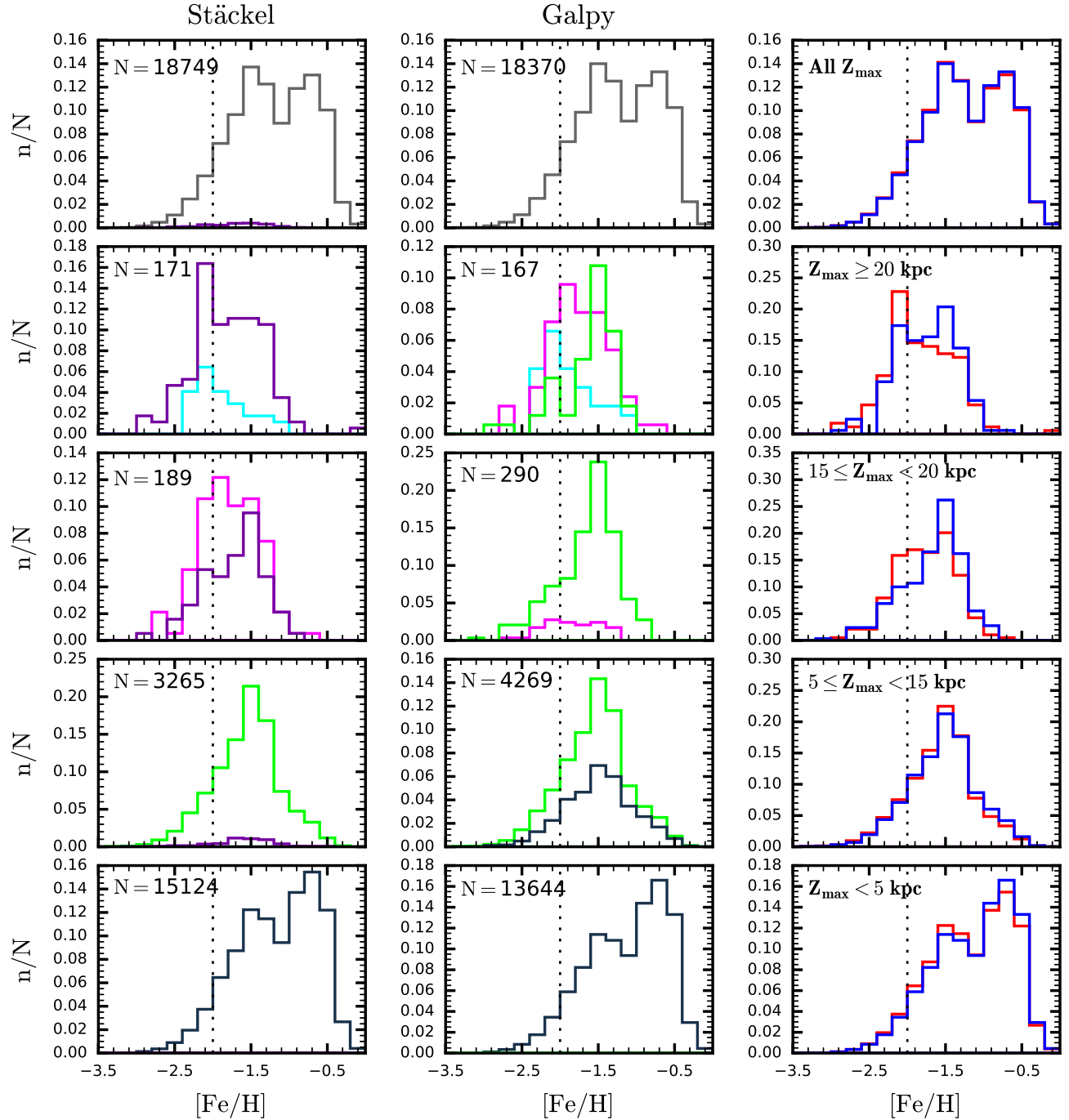


Figure 3. Same as in Figure 2, but for the metallicity distribution functions. The legend for each color is the same as in Figure 1. The vertical dotted line is at [Fe/H] = -2.0 for reference.

in the Stäckel potential, but are also symmetric around $\alpha = 90^\circ$. In particular, we notice that some portion of stars (green dots in the second from the top in the right panels) in the range $5 \leq Z_{\max} < 15$ kpc in the Stäckel potential reach the region of $Z_{\max} > 20$ kpc in the Galpy potential. The unbound stars (shown in purple in the left panels) are more populated in the region of $\alpha > 90^\circ$.

Figure 2 shows histograms of the rotation velocities in different bins of Z_{\max} for the Stäckel (left panels) and the Galpy (middle panels) potential, respectively. The right

column of panels is the distribution of rotation velocity for all stars in a given bin of Z_{\max} for the Stäckel (red line) and the Galpy potential (blue line). The general trend in this figure, except for the region ($Z_{\max} < 5$ kpc) in which thick-disk stars dominate, is that the distribution of rotation velocities of bound stars (the green, magenta, blue, and black histograms) is symmetric around $V_\phi = 0$, and the net rotational velocity is nearly zero in both potentials. On the other hand, the rotational motion of the unbound stars (purple histogram in the left

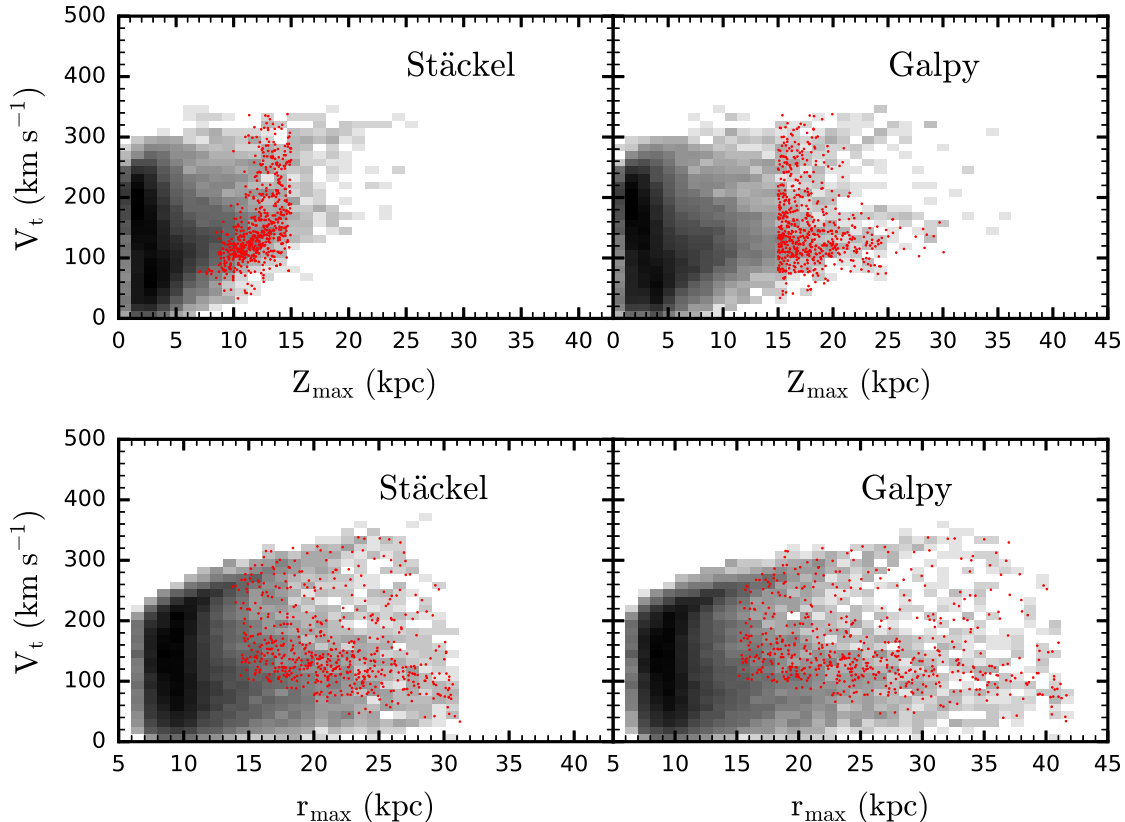


Figure 4. Distribution of tangential velocity (V_t) as a function of Z_{\max} (top panels) and r_{\max} (bottom panels) for the Stäckel (left panels) and the Galpy (right panels) potential, respectively. In these plots, bound stars are displayed with the number density map on a log-10 based scale (low to high from bright to dark), whereas red dots mark stars with $Z_{\max} < 15$ kpc from the Stäckel potential and with $Z_{\max} > 15$ kpc from the Galpy potential.

panels) in the Galpy potential above $Z_{\max} = 5$ kpc is predominantly retrograde, regardless of the Z_{\max} range. As can be seen in the right-column panels, the result is that the V_ϕ distribution (red histogram) of the bound stars in the Stäckel potential exhibits a retrograde motion (blue histogram) over $Z_{\max} > 15$ kpc, while the net rotation velocity of bound stars in the Galpy potential is nearly zero. This leads us to conclude that the pronounced differences in the V_ϕ distribution over Z_{\max} between the two potentials are primarily caused by the absence of the unbound stars in the Galpy potential.

The MDFs are shown in Figure 3, in different bins of Z_{\max} derived from the Stäckel (left panels) and the Galpy (middle panels) potentials, respectively. The right-column panels are the MDFs for the bound stars in each range of Z_{\max} for the Stäckel (red line) and the Galpy (blue line) potential, respectively. In the left-column panels of the figure, we note that the MDF for bound stars in the Stäckel potential exhibits a transition from relatively metal-rich ($-1.7 \leq [\text{Fe}/\text{H}] < -1.0$) to more metal-poor ($[\text{Fe}/\text{H}] < -1.7$) beyond $Z_{\max} = 15$ kpc. In contrast, the unbound stars (purple distribution) in the Galpy potential exhibit a peak of the MDF in the metal-poor region over $Z_{\max} = 20$ kpc, although there is still some fraction of stars in the metal-rich region.

For the Galpy potential, the shape of the MDF does not change much between $Z_{\max} = 5$ and 20 kpc. However, beginning at $Z_{\max} > 20$ kpc, the MDF exhibits a larger fraction of more metal-poor stars, with substan-

tial numbers of relatively high-metallicity ($[\text{Fe}/\text{H}] > -1.7$) stars, displaying two apparent peaks. Interestingly, the metal-rich stars are contributed from the stars in the range $5 \leq Z_{\max} < 15$ kpc in the Stäckel potential. Consequently, the metallicity shift occurs at larger Z_{\max} (> 20 kpc) for the Galpy potential than for the Stäckel potential. The difference in the V_ϕ distribution and MDF over Z_{\max} between the two potentials suggests that the adoption of the Galpy potential may result in a different interpretation of the Galactic halo properties, compared to that from obtained with the Stäckel potential.

4.2. Differences in Halo Properties from the DR12 Sample

In the previous section, we demonstrated that the distribution of stars changes with Z_{\max} , depending on the assumed potential. Accordingly, so do the V_ϕ distributions and the MDFs. As a result, the transition region between the inner and outer halos inferred from the shift of the distribution of V_ϕ and $[\text{Fe}/\text{H}]$ over Z_{\max} occurs in different location for these potentials. Here, we examine these characteristics in more detail with a larger extended sample from the SDSS DR12.

Figure 4 presents a logarithmic density map of V_t versus Z_{\max} (top panels) and r_{\max} (bottom panels) for the Stäckel (left panels) and Galpy (right panels) potentials. In this figure, the red dots are stars in the range $Z_{\max} > 15$ kpc in the Galpy potential and in the region $Z_{\max} < 15$ kpc in the Stäckel potential. From the top pan-

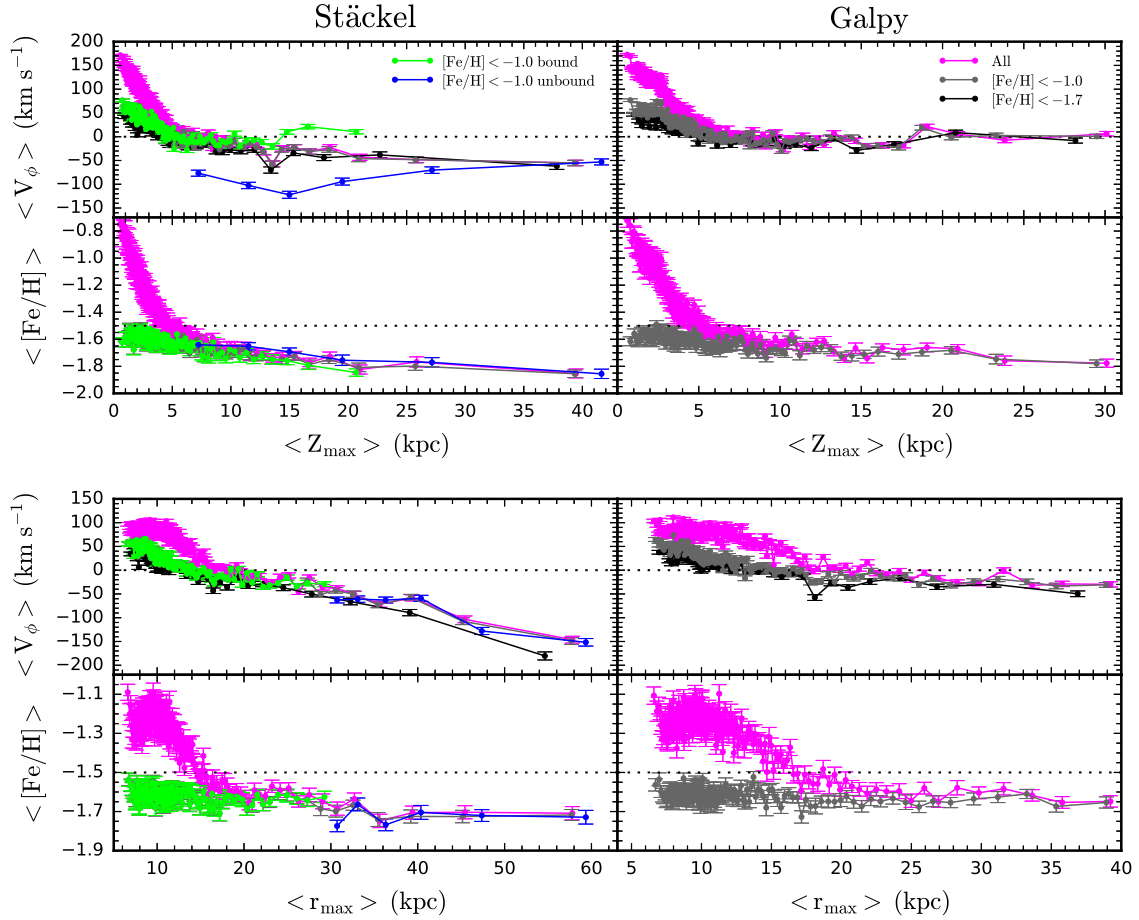


Figure 5. Left panels: profiles of mean rotational velocity ($\langle V_\phi \rangle$) and mean $[\text{Fe}/\text{H}]$ ($\langle [\text{Fe}/\text{H}] \rangle$), as a function of mean Z_{\max} (top two panels) and mean r_{\max} (bottom two panels) for the Stäckel potential. Right panels: same as in the left panels, but for the Galpy potential. Each mean value is obtained by passing a box of 130 stars in Z_{\max} and r_{\max} . As denoted in the legends, the magenta curve is for all stars, the gray curve for stars with $[\text{Fe}/\text{H}] < -1.0$, and the black curve for stars with $[\text{Fe}/\text{H}] < -1.7$. Green and blue lines in the left panels represent trends of the mean values calculated for bound and unbound stars from the Stäckel potential, respectively. The error bar in V_ϕ is the standard error of 20 Monte Carlo samples (see the text in Section 5.1 for more detailed information) and the one in $[\text{Fe}/\text{H}]$ is derived from 100 bootstrap resamples of 130 stars in each bin.

els of the figure, we note that the displacement of stars in the Galpy potential generally reaches larger Z_{\max} (~ 35 kpc) than for the Stäckel potential. One notable feature is that the stars around $V_t \sim 100$ km s $^{-1}$ in the Galpy potential exhibit remarkable excursions to higher Z_{\max} compared to the Stäckel potential. These stars are mostly found close to $\alpha = 90^\circ$, as can be inferred from the right panels of Figure 1, and have larger V_θ velocity components. Thus, stars with larger V_θ reach higher Z_{\max} . Here, as $\alpha \sim 90^\circ$ and $V_t \sim 100$ km s $^{-1}$, we can infer from the equation given in Section 3 that $V_\theta \sim 100$ km s $^{-1}$ and $V_\phi \sim 0$ km s $^{-1}$. Hence, the distribution of stars between both potentials with Z_{\max} changes primarily due to those stars. For example, the stars shown as red dots in Figure 4 in the region of $Z_{\max} < 15$ kpc in the Stäckel potential reach up to $Z_{\max} = 30$ kpc and many of them are located in the range $15 < Z_{\max} < 25$ kpc in the Galpy potential. As seen in the middle panels of Figure 3, stars with $5 \leq Z_{\max} < 15$ kpc in the Stäckel potential are dominated by objects with $[\text{Fe}/\text{H}] > -1.7$. Because these stars extend up to $Z_{\max} = 20$ kpc in the Galpy potential, the shift of the MDF to lower $[\text{Fe}/\text{H}] < -1.7$ occurs above $Z_{\max} = 20$ kpc in the Galpy potential.

By way of contrast, there is no significant variation in the overall distribution of stars over r_{\max} between the two potentials, as can be seen in the bottom panels of Figure 4.

Figure 5 shows profiles of the mean rotational velocity ($\langle V_\phi \rangle$) and mean $[\text{Fe}/\text{H}]$ ($\langle [\text{Fe}/\text{H}] \rangle$), as a function of mean Z_{\max} (top two panels) and mean r_{\max} (bottom two panels) for the Stäckel potential in the left panels, and for the Galpy potential in the right panels. Average values are calculated by passing a box of 130 stars in Z_{\max} and r_{\max} . The error bar in V_ϕ is obtained from 20 Monte Carlo samples (see the text in Section 5.1 for more detailed information); the one in $[\text{Fe}/\text{H}]$ is the standard deviation of 100 bootstrap resamples of 130 stars in each bin. The magenta curve is for all stars, the gray curve for stars with $[\text{Fe}/\text{H}] < -1.0$, and the black curve from stars with $[\text{Fe}/\text{H}] < -1.7$. The green and blue lines in the left panels denote trends of the mean values obtained from bound and unbound stars in the Galpy potential, respectively.

From inspection of the magenta profiles, as a function of Z_{\max} , for the Stäckel potential, we can infer that a transition in both V_ϕ and $[\text{Fe}/\text{H}]$ occurs around $Z_{\max} =$

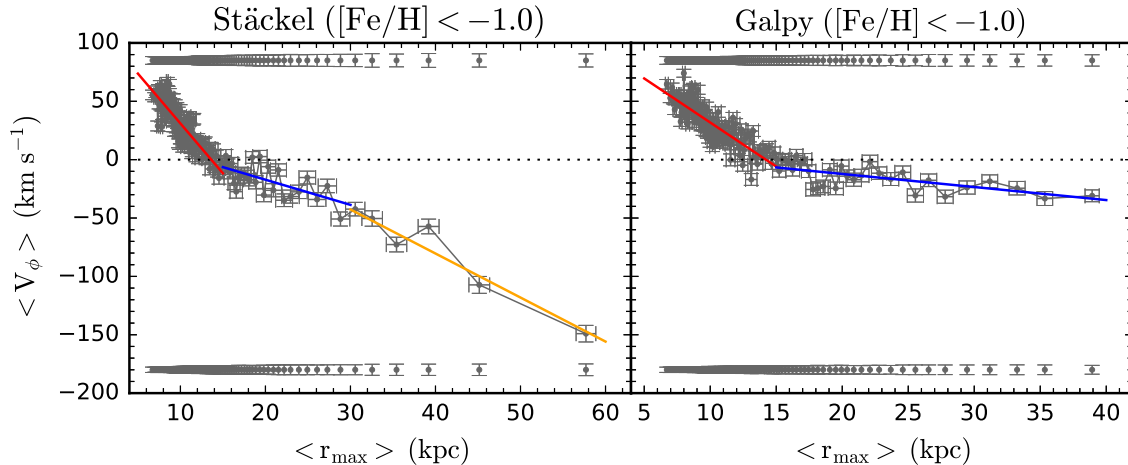


Figure 6. Linear regressions on V_ϕ for stars with $[\text{Fe}/\text{H}] < -1.0$ in the ranges of $r_{\max} < 15$ kpc (red line), $15 \leq r_{\max} < 30$ kpc (blue line), and $r_{\max} \geq 30$ kpc (orange line) for the Stäckel potential (left panel), and $r_{\max} < 15$ kpc (red line) and $r_{\max} \geq 15$ kpc (blue line) for the Galpy potential (right panel). The profile of the rotational velocity is the same as for $[\text{Fe}/\text{H}] < -1.0$ in Figure 5. The upper and lower error bars are for V_r and V_θ in the r_{\max} bins, respectively. The error bars are obtained from 20 Monte Carlo samples (see the text in Section 5.1).

15 kpc. At the largest Z_{\max} distance, $\langle V_\phi \rangle = -60$ km s⁻¹ and $\langle [\text{Fe}/\text{H}] \rangle = -1.9$. On the other hand, for the Galpy potential, the transition appears to exist only for $[\text{Fe}/\text{H}]$ above $Z_{\max} = 20$ kpc, where $\langle [\text{Fe}/\text{H}] \rangle = -1.8$; the mean rotation velocity exhibits a flat (nearly zero) behavior.

In Section 4.1, it was shown that the retrograde motions of stars in the Stäckel potential are almost independent of Z_{\max} . This behavior is investigated in detail by looking into the left column of panels in Figure 5, which show the mean rotational velocity and $[\text{Fe}/\text{H}]$ for bound stars with a green line and for unbound stars with a blue line. Inspection of these panels reveals that the unbound stars show a retrograde motion at all Z_{\max} , whereas the bound stars exhibit a prograde motion below $Z_{\max} = 5$ kpc and almost zero net rotation velocity beyond that distance. We also note that the mean $[\text{Fe}/\text{H}]$ profiles differ between the two groups as well. Because this distinction arises due to differences in the energy of the stellar orbits between the bound and unbound stars, we suggest that r_{\max} , which is more correlated with energy, is the more appropriate parameter to separate the IHP from the OHP, identifying stellar populations with distinct chemistry and kinematics in the Galactic halo.

The lower left-hand panels of Figure 5 show the mean rotation velocity and $[\text{Fe}/\text{H}]$, as a function of r_{\max} , from the Stäckel potential; there is a clearly different behavior seen between the bound (green line) and unbound (blue line) stars with $[\text{Fe}/\text{H}] < -1.0$ at $r_{\max} = 30$ kpc. The mean rotation velocity of bound stars shows a prograde motion in the region $r_{\max} < 15$ kpc, becomes less than zero at $r_{\max} = 15$ kpc, and decreases slightly (to $V_\phi \sim -30$ km s⁻¹) up to $r_{\max} = 30$ kpc. The mean rotational velocity of unbound stars declines noticeably with increasing r_{\max} from $r_{\max} = 30$ kpc down to $V_\phi \sim -150$ km s⁻¹ at $r_{\max} = 60$ kpc. The mean $[\text{Fe}/\text{H}]$ profile also exhibits an abrupt change around $r_{\max} = 30$ kpc, exhibiting $[\text{Fe}/\text{H}] = -1.7$ above this distance.

In contrast, the mean rotation velocity (gray symbols in the right panels of Figure 5) of the stars with $[\text{Fe}/\text{H}] < -1.0$ in the Galpy potential decreases only a little beyond $r_{\max} = 15$ kpc, and remains almost flat at $V_\phi \sim -30$ km

s⁻¹, which is similar to the Stäckel potential (green dots in the left panel) up to that distance. Additionally, it is interesting to see that there is no change in the mean $[\text{Fe}/\text{H}]$ with increasing r_{\max} .

To further clarify the transition of V_ϕ with r_{\max} , we divided r_{\max} into the ranges of $r_{\max} < 15$ kpc, $15 \leq r_{\max} < 30$ kpc, and $r_{\max} \geq 30$ kpc for the Stäckel potential, and $r_{\max} < 15$ kpc, $r_{\max} \geq 15$ kpc for the Galpy potential, based on inspection of Figure 5. We then applied linear regressions of V_ϕ for stars with $[\text{Fe}/\text{H}] < -1.0$ in each region, as shown in Figure 6. The profile of the rotational velocity is the same as for $[\text{Fe}/\text{H}] < -1.0$ in Figure 5. We obtained the following means and gradients for the Stäckel potential: $\langle V_\phi \rangle = 29.9 \pm 0.4$ km s⁻¹, $\Delta V_\phi / \Delta r_{\max} = -8.5 \pm 0.4$ km s⁻¹ kpc⁻¹ for $r_{\max} < 15$ kpc; $\langle V_\phi \rangle = -16.8 \pm 1.1$ km s⁻¹, $\Delta V_\phi / \Delta r_{\max} = -2.2 \pm 0.5$ km s⁻¹ kpc⁻¹ for $15 \leq r_{\max} < 30$ kpc; and $\langle V_\phi \rangle = -83.8 \pm 2.8$ km s⁻¹, and $\Delta V_\phi / \Delta r_{\max} = -3.8 \pm 0.5$ km s⁻¹ kpc⁻¹ for $r_{\max} \geq 30$ kpc. For the Galpy potential, we obtained: $\langle V_\phi \rangle = 31.3 \pm 0.4$ km s⁻¹, $\Delta V_\phi / \Delta r_{\max} = -7.5 \pm 0.4$ km s⁻¹ kpc⁻¹ for $r_{\max} < 15$ kpc; and $\langle V_\phi \rangle = -14.6 \pm 1.0$ km s⁻¹, $\Delta V_\phi / \Delta r_{\max} = -1.1 \pm 0.3$ km s⁻¹ kpc⁻¹ for $r_{\max} \geq 15$ kpc. Figure 6 shows a clear discontinuity in the trend of V_ϕ at $r_{\max} \geq 30$ kpc for the Stäckel potential, but we do not see such a trend for the Galpy potential. In Figure 6, the upper and lower error bars for V_r and V_θ in r_{\max} bins are shown for reference. The error bars of r_{\max} , V_ϕ , V_r , and V_θ are the standard deviations for 20 Monte Carlo samples in each bin, respectively (see the text in Section 5.1).

In order to confirm the results from consideration of the transition region described above, Figure 7 presents the distributions of rotation velocities and metallicities for stars with $[\text{Fe}/\text{H}] < -1.0$ in different r_{\max} bins. In the first column of panels, the peak in the distribution of rotation velocities from the Stäckel potential (red line) is prograde in the range of $r_{\max} < 15$ kpc, with a small shift to retrograde motion from $r_{\max} = 15$ to 30 kpc. However, the fraction of stars with large retrograde motions ($V_\phi < -200$ km s⁻¹) increases above $r_{\max} = 30$

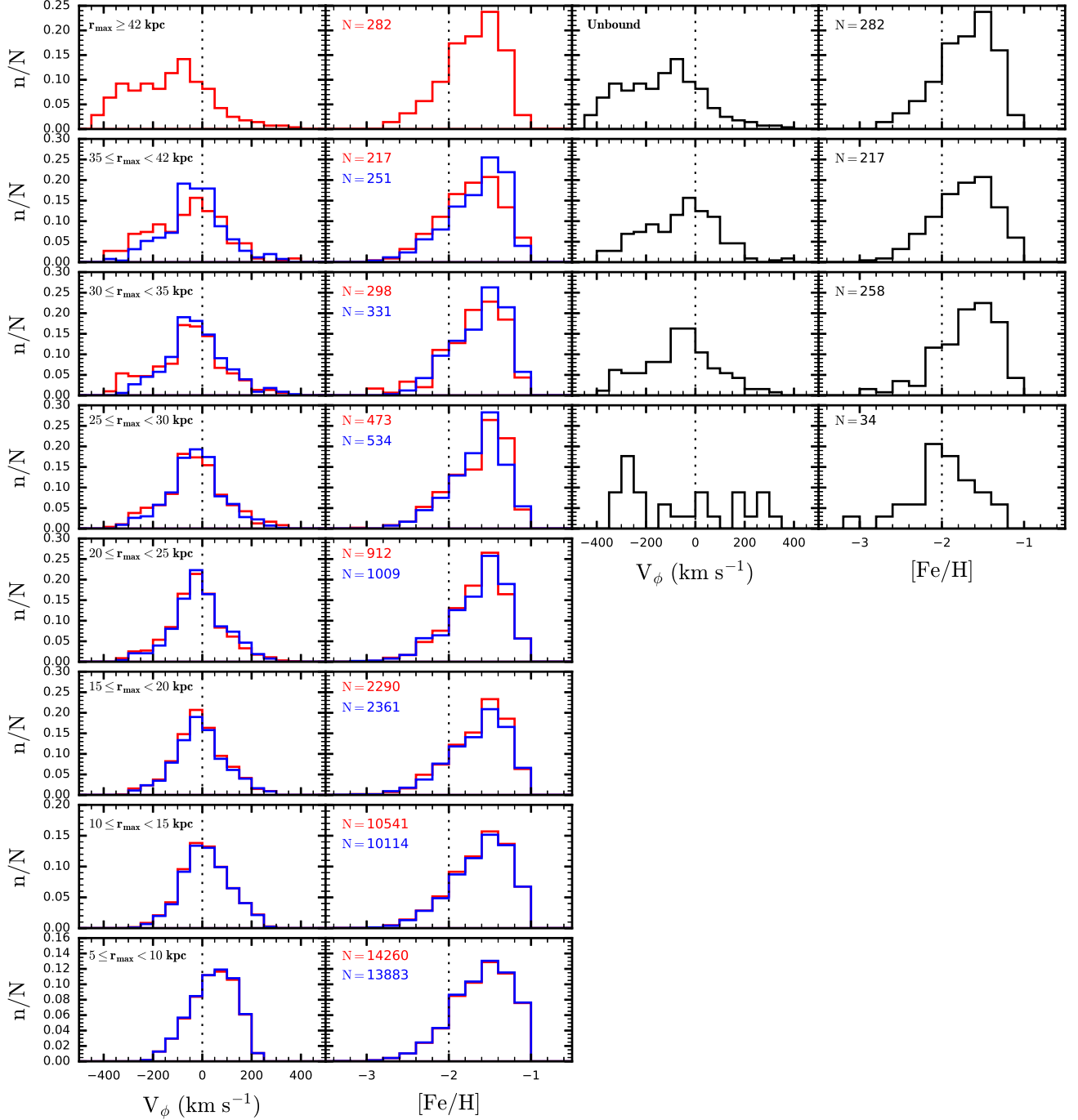


Figure 7. Distribution of rotational velocities and metallicities for all stars (first and second columns of panels) and for unbound stars in the Galpy potential (third and fourth columns). Here, N is the total number of stars in each panel. Only stars with $[\text{Fe}/\text{H}] < -1.0$ are considered. Histograms are shown in red and blue lines for the Stäckel and the Galpy potentials, respectively.

kpc, and the majority of stars in the region of $r_{\text{max}} \geq 42$ kpc possess retrograde motions. This trend is due primarily to the unbound stars in the Galpy potential, as can be seen in the third column of panels in Figure 7. In accordance with this behavior, we note in the second column of panels that the fraction of metal-poor stars becomes relatively larger in the range of $r_{\text{max}} > 30$ kpc, even though the peak of the distribution is still at $[\text{Fe}/\text{H}] = -1.5$.

By contrast, both the distributions of rotation veloci-

ties and metallicities from the Galpy potential shown in the blue line in Figure 7 do not present any remarkable shifts in the first and second column of panels. This leads to a conclusion that the halo stars analyzed with the orbital parameters derived from the Stäckel potential exhibit at least two components, while only one component is evident when the Galpy potential is employed. Consequently, the interpretation of the halo structure can be changed by the nature of the adopted Galactic potential. Based on these results, we suggest a transition distance

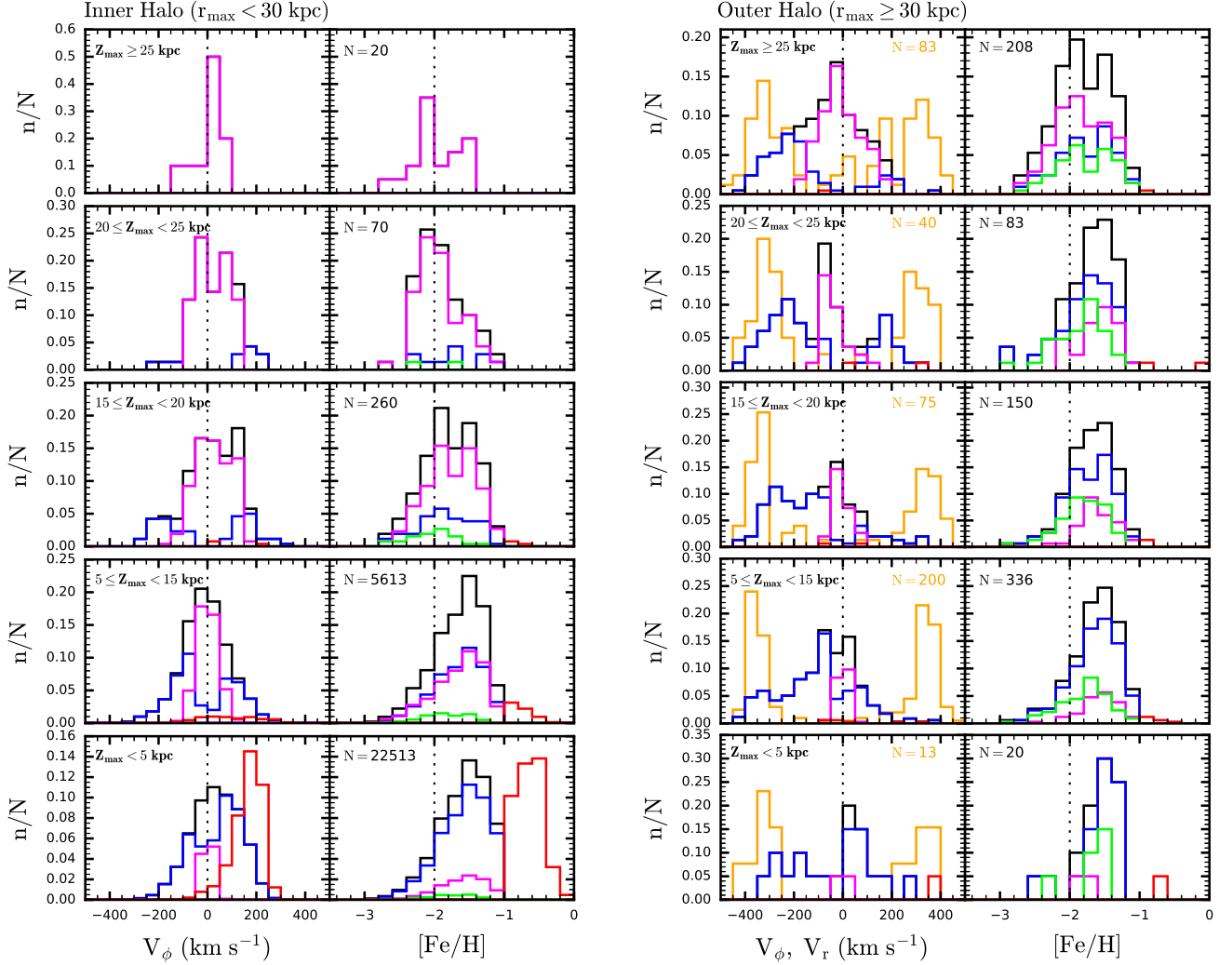


Figure 8. Distribution of rotation velocities and MDFs for the IHP (left two columns) and the OHP (right two columns), separated at $r_{\max} = 30$ kpc from the Stäckel potential, in various Z_{\max} bins, as listed in each panel. Here, N is the total number of stars in each bin. Only stars with $[\text{Fe}/\text{H}] < -1.0$ are taken into account. The magenta histogram is for stars with a large orbital inclination ($i > 60^\circ$), the blue for the stars with small inclinations ($i < 60^\circ$), and black is for all stars. The stars in the range $V_\phi < -150$ km s $^{-1}$ are represented by green lines in the MDFs. The red histogram indicates the likely thick-disk stars ($[\text{Fe}/\text{H}] \geq -1.0$) in our sample. The orange histogram in the first column of the right-two column panels is the V_r distribution of the relatively more metal-rich ($[\text{Fe}/\text{H}] > -1.7$) stars in the OHP.

of $r_{\max} = 30$ kpc from the inner to the outer halo and adopt it as a reference point to distinguish the IHP from the OHP.

4.3. Properties of the IHP and OHP

For local stars at a given energy, the stars with a large orbital inclination and high tangential velocity have orbital motions with high Z_{\max} , while those with a small orbital inclination and high tangential velocity show rotational motions closer to the disk with low Z_{\max} . On the other hand, most stars with high radial velocities possess low Z_{\max} , regardless of their orbital inclination. As seen in Figure 5, the metallicity profile exhibits a more obvious transition with Z_{\max} than r_{\max} . This implies that a parent satellite galaxy (or possibly a globular cluster) contributing metal-poor stars with high Z_{\max} is different from one donating stars with low Z_{\max} . Thus, investigation of the relationship between the orbital parameters (Z_{\max}) and metallicity in different ranges of energy or

r_{\max} can provide valuable information on the dynamical structure of the Galactic halo.

Figure 8 shows the distribution of rotation velocities and metallicities of the IHP (left-two columns) and the OHP (right-two columns) divided at $r_{\max} = 30$ kpc, in different bins of Z_{\max} , calculated from the Stäckel potential for the DR12 sample. The cut of $r_{\max} = 30$ kpc was derived based on the change in the shape of the V_ϕ distribution for the stars in the range $[\text{Fe}/\text{H}] < -1.0$, as described in the previous subsection. In the figure, the magenta histogram is for the stars with large orbital inclination ($i > 60^\circ$), the blue histogram for the stars with small inclination ($i < 60^\circ$), and the black histogram for all stars. The green distribution in the panels for the MDF indicates the stars in the range $V_\phi < -150$ km s $^{-1}$. The red histogram is constructed from stars with $[\text{Fe}/\text{H}] \geq -1.0$ in our sample. The orange histogram is the V_r distribution of metal-rich ($[\text{Fe}/\text{H}] > -1.7$) stars in the OHP.

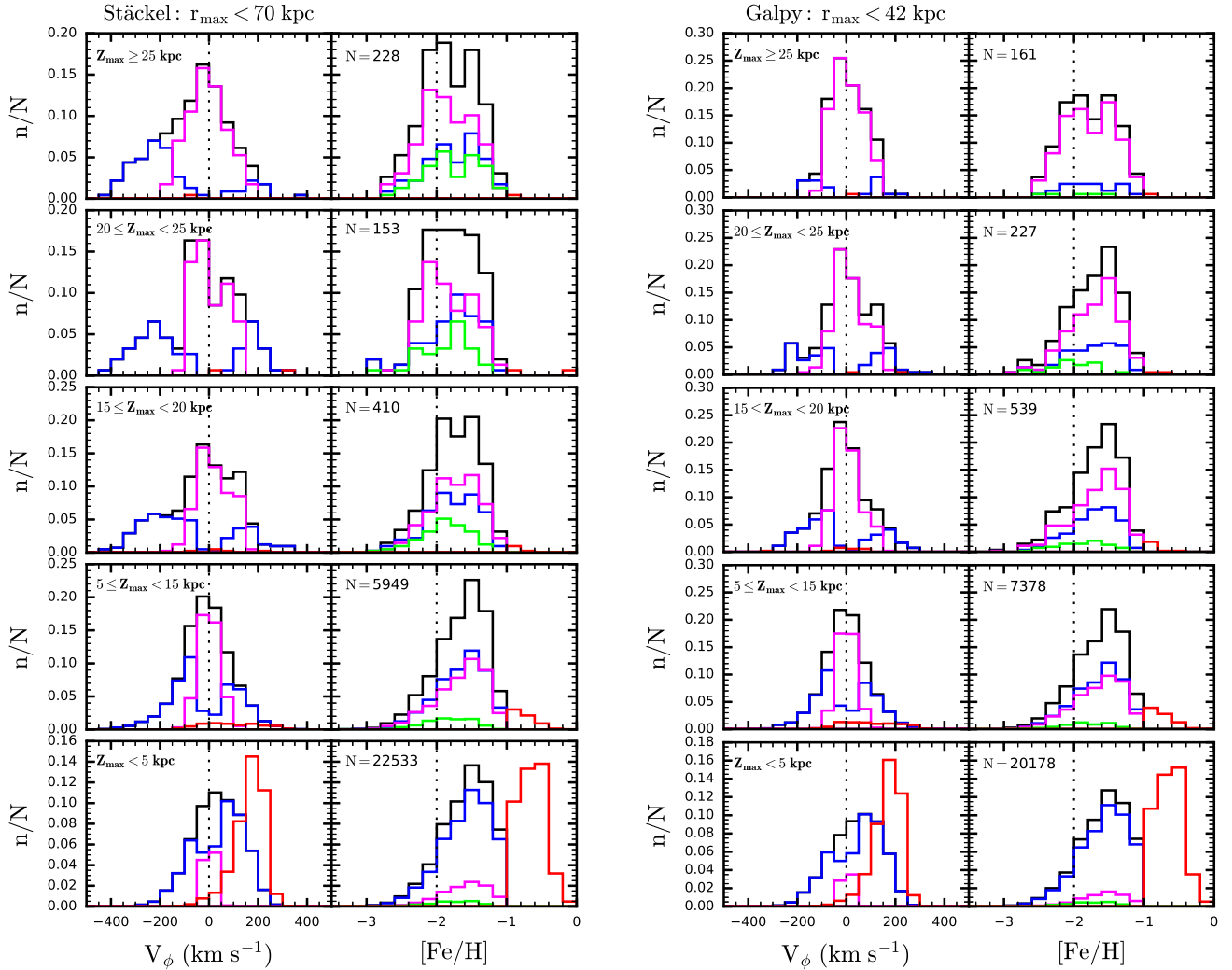


Figure 9. Same as in Figure 8, but for the Stäckel (left two columns) and the Galpy potential (right two columns), without separating the stars into the IHP and OHP components.

Inspection of the MDFs of the IHP in Figure 8 reveals that metal-poor ($[\text{Fe}/\text{H}] < -1.7$) stars start to dominate in the region above $Z_{\text{max}} = 15$ kpc. These metal-poor stars have relatively large orbital inclinations (magenta histogram) and a large dispersion in V_ϕ . In this region ($Z_{\text{max}} > 15$ kpc), the net rotational velocity is nearly zero, as can be seen in the left column of the panels. On the other hand, metal-rich ($[\text{Fe}/\text{H}] > -1.7$) stars dominate below $Z_{\text{max}} = 15$ kpc. The number of stars with high orbital inclinations (magenta histogram) is similar to the number of stars with small orbital inclinations (blue histogram) in the range $5 \leq Z_{\text{max}} < 15$ kpc, while most stars in the region of $Z_{\text{max}} < 5$ kpc have disk-like motions, as can be seen from the red histogram constructed from stars with $[\text{Fe}/\text{H}] \geq -1.0$; these are likely members of the metal-weak thick-disk population. The distribution of the rotation velocity in the range of $5 \leq Z_{\text{max}} < 15$ kpc is symmetric about $V_\phi = 0$, while the number of stars with prograde motions increases in the region of $Z_{\text{max}} < 5$ kpc, compared to the numbers of stars with retrograde motions.

In the OHP shown in the right two panels of Figure 8, it is clear that most stars exhibit retrograde rotation,

with $V_\phi < -150$ km s $^{-1}$, independent of Z_{max} , although there are some stars with prograde motions. A large portion of these stars have low orbital inclinations (blue histogram). In the range of $Z_{\text{max}} \geq 25$ kpc, the stars near $V_\phi = 0$ have high orbital inclinations, while in the range of $Z_{\text{max}} < 25$ kpc, the stars exhibit a large V_ϕ velocity dispersion regardless of their Z_{max} cuts.

It is also interesting to note that, in the MDFs of the OHP, there is a greater fraction of metal-poor ($[\text{Fe}/\text{H}] < -1.7$) stars with large retrograde motions ($V_\phi < -150$ km s $^{-1}$) than metal-rich ($[\text{Fe}/\text{H}] > -1.7$) stars, regardless of Z_{max} (see the green histograms of the right two columns of Figure 8). We also notice that metal-poor stars become more dominant in the region of $Z_{\text{max}} \geq 25$ kpc, while metal-rich stars become more populous in the range of $Z_{\text{max}} < 25$ kpc. This feature is slightly different from the IHP, which shows that the dominance of the metal-poor stars appear to occur at $Z_{\text{max}} = 15$ kpc.

The different spatial distributions of the metal-poor stars between the IHP and OHP can be understood as follows. As the most metal-poor stars in the OHP have primarily high inclination with high tangential orbits and high retrograde orbits, they can easily reach above Z_{max}

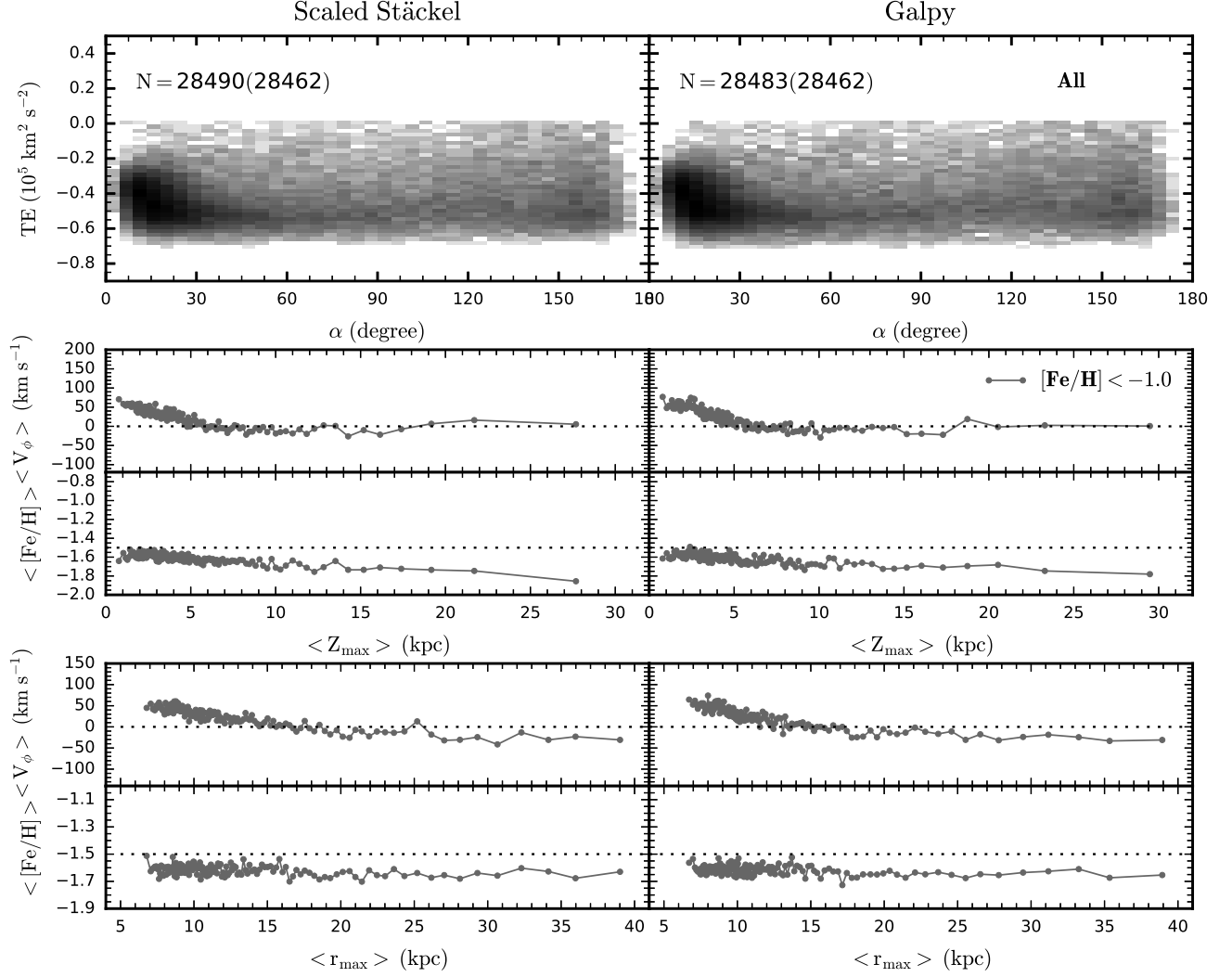


Figure 10. Left panels: distribution of total energy (TE) versus α for all stars (top panel) and profiles of mean rotational velocity and mean $[\text{Fe}/\text{H}]$ for stars with $[\text{Fe}/\text{H}] < -1.0$, as a function of mean Z_{max} (middle two panels) and mean r_{max} (bottom two panels) for the scaled Stäckel potential. Right panels: same as in the left panels, but for the Galpy potential. Numbers in the top panels indicate how many bound stars are in the respective potentials. Numbers in brackets indicate how many stars are bound in both potentials. Maps in the top panels display the number density (low to high from bright to dark) on a log-10 based scale for all stars. Each mean value is obtained by passing a box of 130 stars in Z_{max} and r_{max} .

= 25 kpc, resulting in their occupation of the region $Z_{\text{max}} \geq 25$ kpc. On the other hand, because the more metal-rich stars have strong radial (see the orange histograms in the first of the right-two columns of Figure 8) and retrograde motions, they do not reach high Z_{max} —rather, they reside at lower Z_{max} (< 25 kpc). Generally, at a given energy, stars with high V_{θ} reach higher Z_{max} than those with high V_r ; reaching a distance of $Z_{\text{max}} > 25$ kpc requires more energy. Hence, the OHP stars with high energy and the IHP stars with low energy represent more metal-poor stars beyond $Z_{\text{max}} = 25$ and 15 kpc, respectively.

Figure 9 shows the distribution of rotation velocities and metallicities for the Stäckel (left two columns) and the Galpy potential (right two columns), *without* dividing stars into the IHP and OHP, for the purpose of comparison to Figure 8. As shown in Figure 9, the Stäckel potential exhibits a retrograde motion, with metal-poor stars dominating beyond $Z_{\text{max}} = 15$ kpc, whereas the Galpy

potential only indicates the shift in the MDF above $Z_{\text{max}} > 25$ kpc. We re-emphasize that the reason for the lack of retrograde motions in the Galpy potential, compared to the Stäckel potential, is not because the stars near $\alpha = 90^\circ$ move up to higher Z_{max} , but rather because the stars with large retrograde orbits are not bound to the potential.

4.4. Halo Properties in the Scaled Stäckel Potential Compared to the Galpy Potential

We also carried out an exercise of rescaling the mass distribution of the Stäckel potential to approximately equal that of the Galpy potential, in order to check whether we obtain similar halo properties from the rescaled Stäckel and Galpy potentials. For this exercise, we first set the tidal cutoff radius of the Stäckel potential to 42 kpc, based on the upper limit of < 42 kpc of r_{max} from the Galpy potential, and the disk mass to $M_d = 7.3 \times 10^{10} M_{\odot}$, which is the sum of the bulge and disk

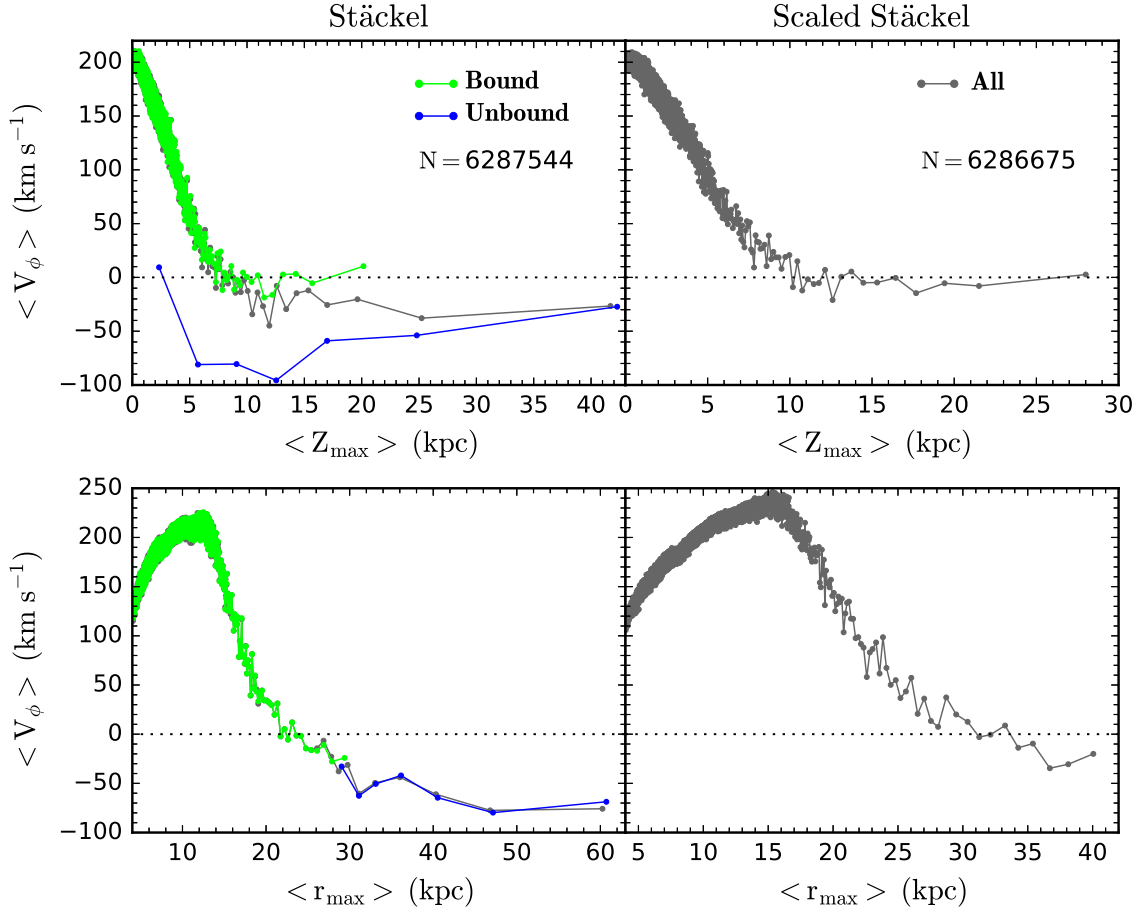


Figure 11. Profiles of mean rotational velocity ($\langle V_\phi \rangle$) for stars in the RVS sample drawn from *Gaia* DR2. Left panels: profiles of mean V_ϕ , as a function of mean Z_{\max} (top panel) and mean r_{\max} (bottom panel), for the Stäckel potential. Right panels: same as in the left panels, but for the scaled Stäckel potential. Each mean value is obtained by passing a box of 130 stars in Z_{\max} and r_{\max} . Here, N is the total number of bound stars in each potential. As denoted in the legends, the gray curve is for all stars. The green and blue lines in the left panels represent trends of the mean values calculated for bound and unbound stars from the scaled Stäckel potential, respectively.

masses from the Galpy potential. We then determined the central density value of $\rho_0 = 1.99 \times 10^7 M_\odot \text{ kpc}^{-3}$, by adjusting that of the halo to make the depth of the scaled Stäckel potential approximately equal to that of the Galpy potential.

Figure 10 shows the distribution of TE versus α for all stars (top panel), along with profiles of the mean rotational velocity ($\langle V_\phi \rangle$) and mean $[\text{Fe}/\text{H}]$ ($\langle [\text{Fe}/\text{H}] \rangle$) for stars with $[\text{Fe}/\text{H}] < -1.0$ as a function of mean Z_{\max} (middle two panels) and mean r_{\max} (bottom two panels) for the scaled Stäckel potential (left panels) and for the Galpy potential (right panels). Average values are calculated by passing a box of 130 stars in Z_{\max} and r_{\max} . The figure clearly demonstrates that we obtain nearly identical halo properties from both the scaled Stäckel and Galpy potentials. This confirms that the different characteristics of the Galactic halo between the Stäckel and Galpy potentials stem primarily from the different potential depths.

4.5. Retrograde Motion Signature from the Radial Velocity Spectrometer Sample of *Gaia* DR2

In order to investigate the reality of the claimed retrograde motion in the Stäckel and scaled Stäckel potentials, we have also made use of a sample of stars with

available radial velocity measurements from the radial velocity spectrometer (RVS) in *Gaia* DR2. We first selected stars satisfying $\pi/\sigma_\pi > 4$ and proper motion errors less than 1.0 mas yr^{-1} in the RVS sample from *Gaia* DR2, using distances derived by Schönrich et al. (2019), who estimated the Bayesian distance for the RVS stars in *Gaia* DR2.

Figure 11 shows profiles of the mean rotational velocity ($\langle V_\phi \rangle$), as a function of mean Z_{\max} (top panel) and mean r_{\max} (bottom panel) for the Stäckel potential in the left panels, and for the scaled Stäckel potential in the right panels. Average values were calculated by passing a box of 130 stars in Z_{\max} and r_{\max} . The gray curve is for all stars. The green and blue lines in the left panels denote trends of the mean values obtained from bound and unbound stars in the scaled Stäckel potential, respectively. Figure 11 verifies that RVS sample of *Gaia* DR2 also shows the signature of retrograde motion for $r_{\max} \geq 30$ kpc, consistent with our result for the Stäckel potential. The left column of panels in Figure 11 also reveal that the rotational velocity depends more strongly on r_{\max} than on Z_{\max} .

5. IMPACTS OF DISTANCE ERROR AND SELECTION BIAS ON DERIVED ORBITAL PARAMETERS

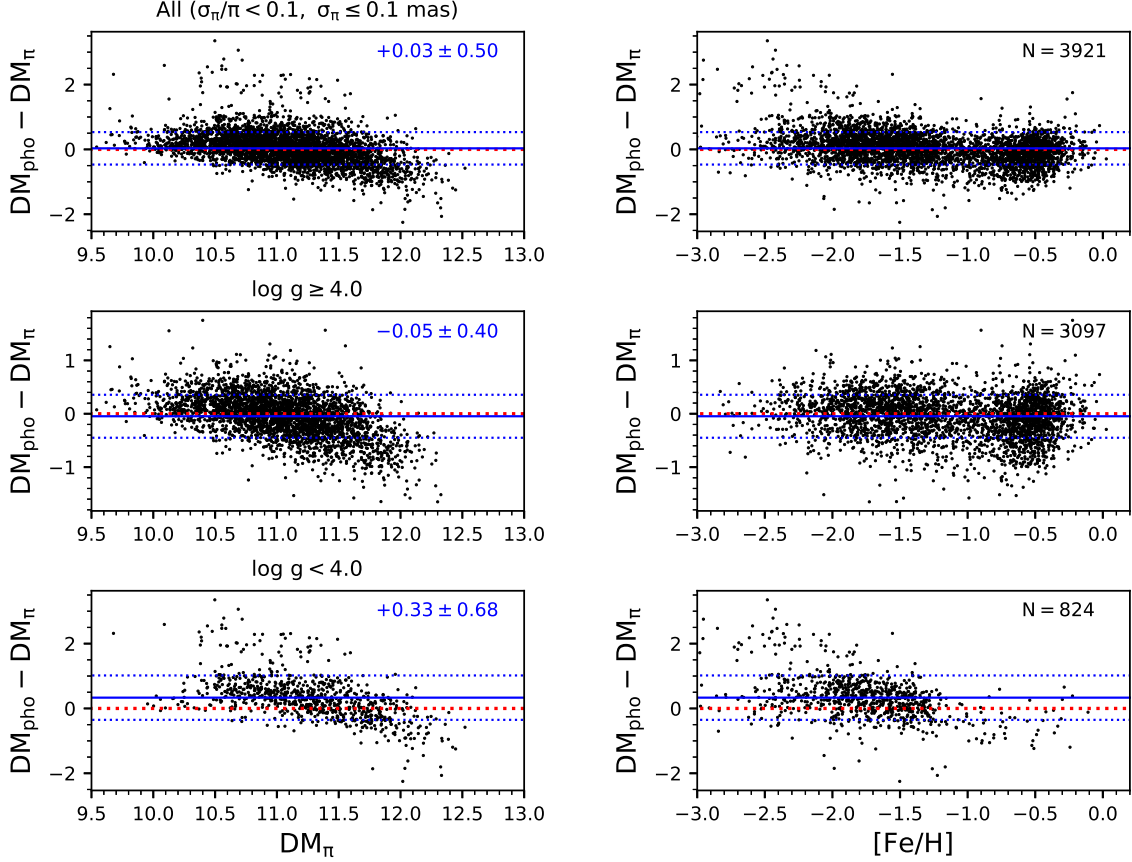


Figure 12. Comparison of our photometric distances (DM_{pho}) and those (DM_{π}) of the *Gaia* DR2. Top panels are for all stars, middle for stars with $\log g \geq 4.0$, and bottom for those with $\log g < 4.0$ as a function of distance modulus (left) and metallicity (right). We used distances corrected by the zero-point offset of -0.029 mas and considered only stars in the ranges of $\sigma_{\pi}/\pi < 0.1$ and $\sigma_{\pi} \leq 0.1$ mas. Numbers in the top right areas of the left and right panels are the means and standard deviations of the differences in distance modulus and the number of stars in each panel.

As any systematic error on estimated measured distance and/or metallicity bias in target selection can affect the derived orbital parameters and any interpretation that follows, below we have investigated these possible impacts.

5.1. Impact of Distance Errors

In order to check whether systematic errors exist in our distance estimates, we matched our calibration-star sample from SDSS DR12 with stars in *Gaia* DR2, and selected stars satisfying $\sigma_{\pi}/\pi < 0.1$ and $\sigma_{\pi} \leq 0.1$ mas, where π is the parallax and σ_{π} is the uncertainty in π . Distances from *Gaia* DR2 were derived by inverting parallaxes, corrected for the zero-point offset of -0.029 mas (Lindgren et al. 2018). Figure 12 shows the differences between our photometric distances (DM_{pho}) and those from *Gaia* DR2 (DM_{π}), as a function of distance modulus (left panels) and metallicity (right panels) for: (1) all matched stars (top panels), (2) stars with $\log g \geq 4.0$ (middle panels), and (3) stars with $\log g < 4.0$ (bottom panels). We found a mean offset of 0.03 dex with a scatter of 0.5 dex for all stars, -0.05 dex with a standard deviation of 0.40 dex for stars with $\log g \geq 4.0$, and an offset of 0.33 dex with a scatter of 0.68 dex for stars with $\log g < 4.0$. As can be appreciated from inspection of the figure, even though the mean offset becomes larger for fainter objects, any systematic difference in the distance

is very small. We also note that there is no significant trend with metallicity.

We further examined the V_{ϕ} profile, as a function of Z_{max} and r_{max} , because the different distance scale could result in different derived orbital parameters. First, based on Figure 12, we selected three groups of stars. The first group consists of stars with $\log g \geq 4.0$, which have a negligible distance offset. The second contains the first group plus the stars with $\log g < 4.0$, which are corrected for the distance offset by $+0.33$ dex. The third group comprises stars chosen from our calibration stars, using the selection criteria described in Section 2, with the distance estimate from *Gaia* DR2, including stars that satisfy $\sigma_{\pi}/\pi < 0.2$ and $\sigma_{\pi} \leq 0.1$ mas. The numbers of bound stars for the Stäckel and Galpy potential are 20,779 and 20,400 for the first group, 29,273 and 28,785 for the second group, and 13,564 and 13,296 for the third group, respectively.

Figure 13 shows profiles of the mean rotational velocity ($\langle V_{\phi} \rangle$), as a function of mean Z_{max} (top two panels) and mean r_{max} (bottom two panels), for the three groups of stars with $[Fe/H] < -1.0$ for the Stäckel potential in the left panels, and for the Galpy potential in the right panels. The first, second, and third groups are displayed in green, black, and red colors, respectively. Average values are calculated by passing a box of 130 stars in Z_{max} and r_{max} . Error bars are not plotted, for a more

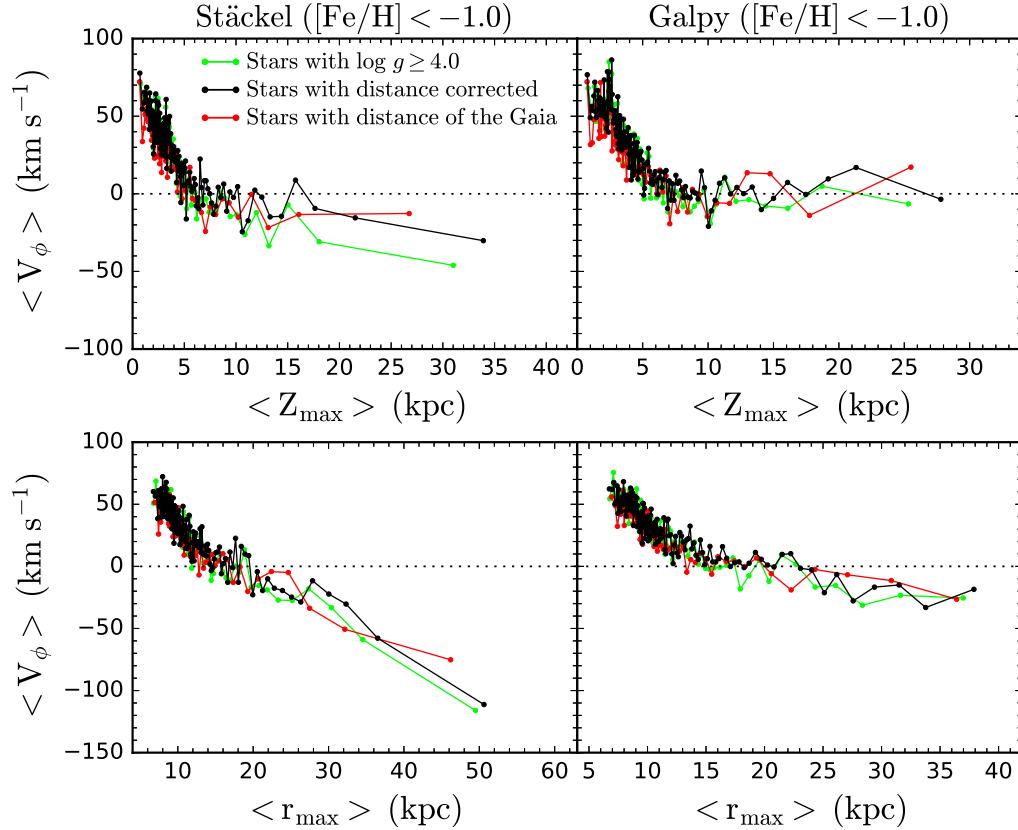


Figure 13. Profiles of the mean rotational velocity ($\langle V_\phi \rangle$), as a function of mean Z_{\max} (top two panels) and mean r_{\max} (bottom two panels) for three groups of stars with $[\text{Fe}/\text{H}] < -1.0$, for the Stäckel potential in the left panels, and for the Galpy potential in the right panels. The first sample consists of stars with $\log g \geq 4.0$, which have a negligible distance offset. The second sample includes stars with $\log g \geq 4.0$ and those with $\log g < 4.0$, corrected for the distance offset by $+0.33$ dex. The third group comprises stars chosen from our calibration stars, using the selection criteria described in Section 2, with the distance estimate from *Gaia* DR2, including stars that satisfy $\sigma_\pi/\pi < 0.2$ and $\sigma_\pi \leq 0.1$ mas. The first, second, and third groups are displayed in green, black, and red colors, respectively. Each mean value is obtained by passing a box of 130 stars in Z_{\max} and r_{\max} .

clear view of the trends. The obvious retrograde motions of all groups for $r_{\max} \geq 30$ kpc in the Stäckel potential indicate that the retrograde motion of our sample is not due to overestimation of our distances.

To assess the impact of observational uncertainties on our derived orbital parameters, we also carried out a comparison of orbital parameters derived for our sample with those of 20 mock samples based on Monte Carlo simulations with an uncertainty of 20% in the distance and quoted uncertainties in the radial velocity and proper motion, assuming a normal error distribution for our sample.

The comparison of our sample with each of the 20 mock samples is performed as follows. For the Stäckel potential, we first separated r_{\max} into three regions, $r_{\max} < 15$ kpc, $15 \leq r_{\max} < 30$ kpc, and $r_{\max} \geq 30$ kpc, and calculated mean V_ϕ and $[\text{Fe}/\text{H}]$ for stars with $[\text{Fe}/\text{H}] < -1.0$ in each region. Similarly, we divided Z_{\max} into two regions, $Z_{\max} < 15$ kpc and $Z_{\max} \geq 15$ kpc, and computed each mean $[\text{Fe}/\text{H}]$ for stars with $[\text{Fe}/\text{H}] < -1.0$. For the Galpy potential, we separated r_{\max} into two regions of $r_{\max} < 15$ kpc and $r_{\max} \geq 15$ kpc, and calculated the mean V_ϕ and $[\text{Fe}/\text{H}]$ for stars with $[\text{Fe}/\text{H}] < -1.0$ in each region. For Z_{\max} , we divided into two regions, $Z_{\max} < 25$ kpc and $Z_{\max} \geq 25$ kpc, and derived each mean $[\text{Fe}/\text{H}]$ for stars with $[\text{Fe}/\text{H}] < -1.0$.

Figure 14 summarizes the comparison. The top panels of the figure show the numbers of bound stars in the Stäckel and Galpy potential, for all stars (left panel) and for only those stars with $[\text{Fe}/\text{H}] < -1.0$ (right panel). A gray star symbol is used for our sample, while the orange star symbols represent the 20 mock samples. The numbers of unbound stars due to observational uncertainties from the 20 simulated samples are, on average, 317 and 584 in the Stäckel and Galpy potential, respectively, for all stars, and 311 and 548 for stars with $[\text{Fe}/\text{H}] < -1.0$. The middle panels display the mean V_ϕ versus the mean $[\text{Fe}/\text{H}]$ for stars with $[\text{Fe}/\text{H}] < -1.0$, in the regions $r_{\max} < 15$ kpc, $15 \leq r_{\max} < 30$ kpc, and $r_{\max} \geq 30$ kpc, in the left panel for the Stäckel potential, and $r_{\max} < 15$ kpc and $r_{\max} \geq 15$ kpc, in the right panel for the Galpy potential. The gray star symbol is for our sample, while the orange star symbols denote the 20 mock samples. Note that as r_{\max} increases, the difference in V_ϕ and $[\text{Fe}/\text{H}]$ between our original sample and the simulated samples becomes larger, but not dramatically so.

The bottom panels represent the distribution of mean $[\text{Fe}/\text{H}]$ of stars with $[\text{Fe}/\text{H}] < -1.0$, in the ranges of $Z_{\max} \geq 15$ kpc and $Z_{\max} < 15$ kpc for the Stäckel potential (left), and $Z_{\max} \geq 25$ kpc and $Z_{\max} < 25$ kpc for the Galpy potential (right). The gray solid line indicates our sample, and the orange solid histogram is for the 20

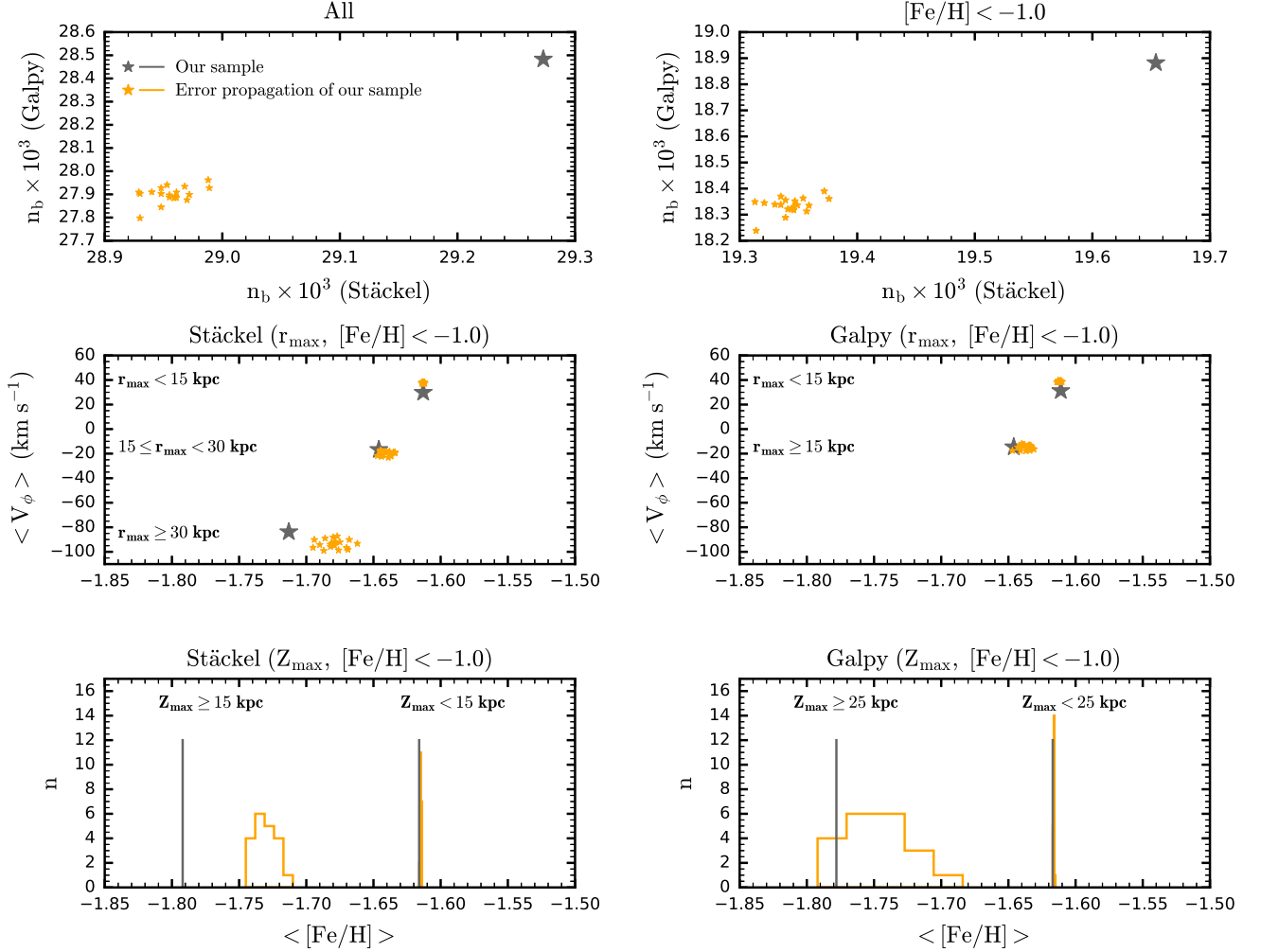


Figure 14. Effects of observational uncertainties based on 20 mock samples obtained from a Monte Carlo simulation. Top panels: mean V_ϕ versus mean $[\text{Fe}/\text{H}]$ for stars with $[\text{Fe}/\text{H}] < -1.0$ in the regions of $r_{\text{max}} < 15$ kpc, $15 \leq r_{\text{max}} < 30$ kpc, and $r_{\text{max}} \geq 30$ kpc for the Stäckel potential (left panels), and $r_{\text{max}} < 15$ kpc and $r_{\text{max}} \geq 15$ kpc for the Galpy potential (right panels). Our sample and each of the 20 mock samples are displayed with the gray star symbols and the orange star symbols, respectively. Bottom panels: distribution of mean $[\text{Fe}/\text{H}]$ for stars with $[\text{Fe}/\text{H}] < -1.0$ in the ranges of $Z_{\text{max}} \geq 15$ kpc and $Z_{\text{max}} < 15$ kpc for the Stäckel potential (left panels), and $Z_{\text{max}} \geq 25$ kpc and $Z_{\text{max}} < 25$ kpc for the Galpy potential (right panels). Our sample and each of the 20 mock samples are displayed with the gray solid line and the orange solid histogram, respectively.

mock samples. In this case, similar to r_{max} , the difference between our sample and the simulated samples is larger for larger Z_{max} for both potentials, but the difference is less than 0.1 dex. Thus, from inspection of Figure 14, we find that there are no large impacts on our results due to uncertainties in the various derived kinematic quantities.

5.2. Impact of Target Selection Effects

In order to check the impact of the target selection effect in our sample on the derived chemo-kinematic features reported in Section 4, we made use of the selection function for SEGUE data provided by Mints & Hekker (2019). The left panel of Figure 15 shows the fractional MDFs, both uncorrected (red line) and corrected (blue line) for SEGUE target selection effects. These MDFs are constructed with the SEGUE stars (Mints & Hekker 2019) that satisfy our stated sampling criteria in Section 2. We then assume that the blue histogram shown in the left panel of Figure 15 represents the MDF that we will scale to, as described below.

Derivation of the selection-corrected (unbiased) MDF for our sample stars proceeds as follows. First, we scaled the fractional unbiased MDF (blue histogram in the left panel of Figure 15) by multiplying by the total number of stars in our sample. This scaled MDF is shown as the orange histogram in the right panel of Figure 15. We then rescaled this MDF (the orange histogram) by multiplying by the ratio of the number of stars of our sample (19,654; the green histogram) to that of the scaled unbiased MDF (2895; the orange histogram). This rescaled MDF is shown as the blue histogram in the right panel of Figure 15. Note that we have restricted the sample to only include the stars with $[\text{Fe}/\text{H}] < -1.0$, which is the metallicity regime of interest for this study. Finally, for each metallicity bin, we calculated the difference in the number of stars between the MDF of our uncorrected sample (green histogram in the right panel of Figure 15) of our sample and the unbiased MDF (blue histogram in the right panel of Figure 15), and randomly draw stars from our sample as many times as required to add to (or

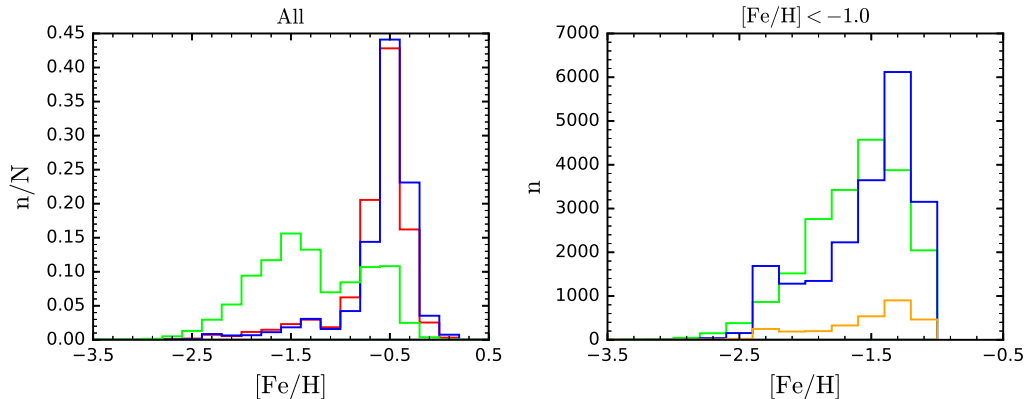


Figure 15. Metallicity distribution functions of stars satisfying our sample selection, from the SEGUE data of Mints & Hekker (2019). Left panel: fractional MDFs, uncorrected (red line) and corrected (blue line) for SEGUE target selection effects, according to Mints & Hekker (2019). Right panel: the orange histogram is a scaled MDF of the corrected MDF (the blue histogram in the left panel), which is obtained by multiplying by the total number of stars in our sample. The blue histogram is a rescaled MDF derived by multiplying the orange histogram by the ratio of the number of stars in our sample (19,654) to that of the scaled and corrected MDF (2895). Note that, in the right panel, we only considered the stars with $[Fe/H] < -1.0$, which is the metallicity range of interest in this study. The green histogram in both panels represents our sample of stars.

subtract from) our sample in order to match the differences in the number of stars between the our uncorrected MDF and the unbiased MDF in each metallicity bin. We carried out this procedure 100 times to obtain 100 different samples.

After construction of an unbiased MDF for our sample, we obtained the mean V_ϕ and $[Fe/H]$ from the 100 simulated samples in the same r_{\max} and Z_{\max} regions as in Figure 14, as shown in Figure 16, for both the Stäckel and Galpy potentials. The top panels of Figure 16 display the mean V_ϕ versus mean $[Fe/H]$ for stars with $[Fe/H] < -1.0$ in the regions of $r_{\max} < 15$ kpc, $15 \leq r_{\max} < 30$ kpc, and $r_{\max} \geq 30$ kpc for the Stäckel potential (left), and $r_{\max} < 15$ kpc, $r_{\max} \geq 15$ kpc for the Galpy potential (right). The gray star symbol indicates our original sample, while the triangle denotes the sample corrected for the target selection effect. From inspection of the figure, it is clear there is almost no difference in V_ϕ between our original sample and the unbiased sample for both potentials. Even though there is a shift to higher metallicity, the magnitude of the shift is less than 0.1 dex, which is smaller than the uncertainty of the metallicity of individual stars. We also note that this small metallicity shift is not correlated with r_{\max} .

The bottom panels represent the distribution of mean $[Fe/H]$ for stars with $[Fe/H] < -1.0$ in the ranges of $Z_{\max} \geq 15$ kpc and $Z_{\max} < 15$ kpc for the Stäckel potential (left), and $Z_{\max} \geq 25$ kpc and $Z_{\max} < 25$ kpc for the Galpy potential (right). The gray solid line is for our original sample and the dotted line is for the unbiased sample. The mean metallicity is shifted to slightly higher values, slightly less so for high Z_{\max} in both potentials. Once again, however, the scale of the shift is less than 0.1 dex. We conclude from this exercise that our sample of stars, even after being corrected for any target selection effect, exhibits clear retrograde motion for $r_{\max} \geq 30$ kpc, as well as the transition in metallicity in both r_{\max} and Z_{\max} that we identified in our original sample.

6. DISCUSSION

Traditionally, the separation of distinct stellar components in the solar neighborhood has been carried out

kinematically, by consideration of the velocity components for individual stars in a Toomre diagram (e.g., Venn et al. 2004; Bonaca et al. 2017). In our study, in order to characterize different stellar components in a local sample of stars, we scrutinized the distribution of rotation velocity as a function of r_{\max} , which is more correlated with the total energy of stars than the orbital parameter Z_{\max} .

Through this investigation, we found that the retrograde motions become as large as $V_\phi = -150$ km s $^{-1}$ at the largest r_{\max} , and that the counter-rotating signature varies more strongly with r_{\max} than with Z_{\max} . These results are consistent with the work of Kafle et al. (2017), who show larger retrograde motion at greater Galactocentric distances, $11 < r < 15$ kpc, based on an in situ sample of main-sequence turn-off stars.

We also identified the transition of one stellar component to another, occurring at $r_{\max} \sim 30$ kpc, in the Stäckel potential. However, because we did not find such a transition in the Galpy potential, we decided to separate the halo stars in our sample into the IHP and OHP at $r_{\max} = 30$ kpc, as derived from the Stäckel potential.

Within the OHP, the more metal-poor stars ($[Fe/H] < -1.7$) exhibit more retrograde motions, independent of Z_{\max} . These stars have characteristics of more polar motions at higher Z_{\max} , which means that they have more tangential motions for high-inclination orbits while possessing more radial motions at lower Z_{\max} . On the other hand, the more metal-rich stars ($-1.7 \leq [Fe/H] < -1.0$) are located over all Z_{\max} , with both radial and retrograde motions, as can be seen in the right-most panel of Figure 8.

The derived chemical and kinematic features of our sample can be understood as follows, in terms of their assembly over Galactic history. Satellite galaxies are affected by both dynamical friction and tidal forces when interacting with the MW, and their stars are stripped off, losing energy and angular momentum. The kinematic properties of stripped stars are considered to be equal to those of their parent galaxies when they are fully accreted into the MW (e.g., Quinn & Goodman 1986; Van den Bosch et al. 1999; Ruchti et al. 2014; Amorisco 2017).

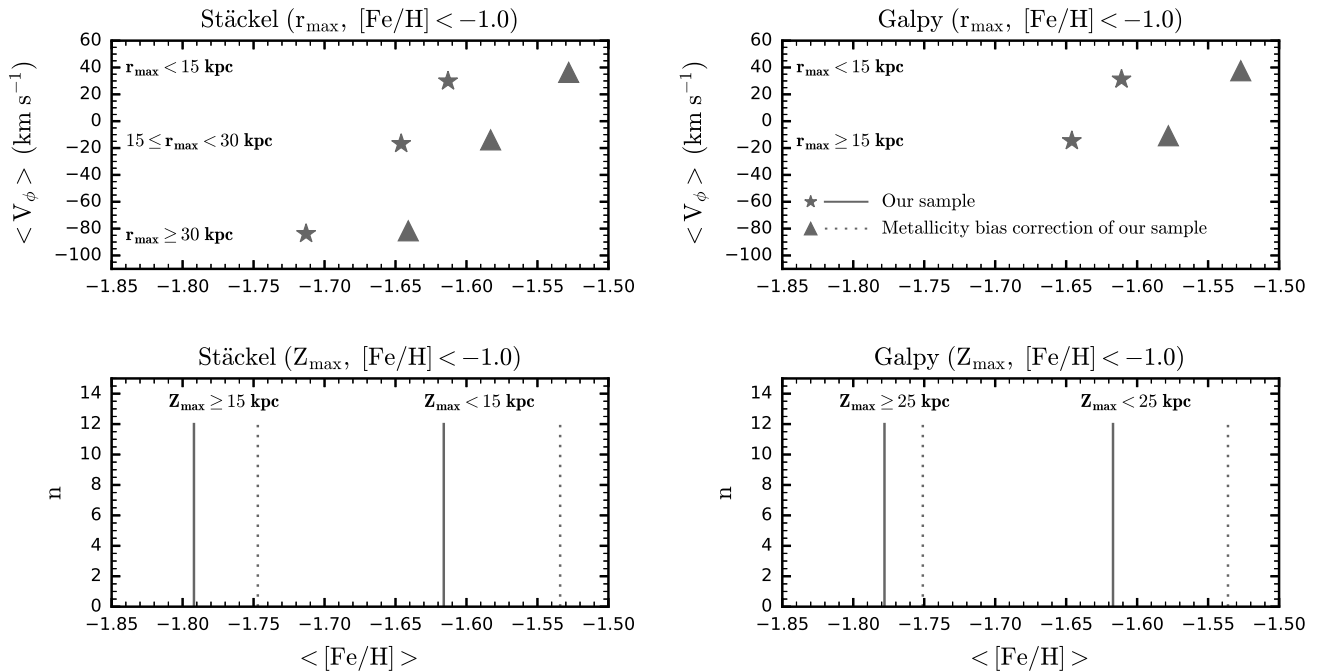


Figure 16. Same as in Figure 14, but for the checks on the impacts of metallicity bias by selection effect of our sample. In the top panels, our sample and the one corrected for metallicity bias by selection effect are displayed with a gray star symbol and triangle, respectively. In the bottom panels, our sample is indicated by a gray solid line, while the one corrected for metallicity bias by selection effect is denoted by a gray dotted line.

Due to weak dynamical friction and self-gravity, an accreted low-mass satellite galaxy loses its stars in outer region of the MW by tidal stripping, whereas a high-mass satellite galaxy sinks farther into the inner region of the MW due to the stronger influence of dynamical friction on its more numerous stars, prior to tidal disruption (Amorisco 2017). In the case of a massive satellite galaxy, with mass on the order of 10% of the MW, the satellite galaxy with a prograde motion contributes more stars to the interior of the MW due to stronger dynamical friction than a satellite galaxy with a retrograde motion (Quinn & Goodman 1986). Results similar to those above have been found in the series of papers from Tissera et al. (2018), and references therein.

The stars stripped off from a lower-mass satellite galaxy with a large orbital inclination and high tangential velocity escape at larger distance from the Galactic plane than those of a high-mass satellite galaxy, regardless of its orbital direction. By comparison, the stars stripped from a satellite galaxy with high radial velocity have small Z_{\max} regardless of its orbital inclination. Consequently, for local stars, the stripped stars from a low-mass satellite galaxy with a retrograde motion are expected to exhibit retrograde motions at the highest (least bound) energies, whereas those from a high-mass satellite galaxy with a prograde motion are expected to move with prograde motions in the inner region of the MW. As a result, if the stars of a low-mass satellite galaxy are more metal-poor than those of a high-mass satellite galaxy (as they are expected to be, due to the difference in their star-formation histories), one could explain the observed relationship between metallicity and rotational velocity as a function of r_{\max} . In addition, as metal-rich stars of our sample have high radial velocities with small Z_{\max} , the transition of metallicity may

be more distinct with Z_{\max} than r_{\max} .

Observationally, our results agree with those inferred from a number of other recent studies. For example, using main-sequence and blue horizontal-branch stars at heliocentric distances ≤ 10 kpc in the SDSS-*Gaia* DR1 catalog, Myeong et al. (2018) show that the more metal-rich stars ($[\text{Fe}/\text{H}] > -1.9$) are well-populated in the high-energy (large r_{\max}) and retrograde regions. Myeong et al. (2019) identify these stars as remnant of the Sequoia Event discernible in the retrograde stellar substructures. The metal-poor stars, however, are more sparsely populated in these regions, in contrast to our result (see the green histograms of the right panel of Figure 8). Similarly, by analyzing main-sequence stars from the same catalog, Belokurov et al. (2018) find that the metal-rich ($[\text{Fe}/\text{H}] > -1.7$) stars exhibit strong overdensities in the region of high V_r velocity, through a multi-Gaussian decomposition of their velocity distributions. This is consistent with our results, as seen in the V_r velocity distribution (shown in orange in Figure 8). Furthermore, the majority of stars associated with *Gaia*-Enceladus, as described by Helmi et al. (2018), are also distributed in the region of $15 < r_{\max} < 30$ kpc and $-200 < V_{\phi} < 10$ km s $^{-1}$, which is a similar to our results. In addition, many stars with high radial velocity ($r_{\max} \geq 30$ kpc) in the study of Belokurov et al. (2018) are considered to be stripped from *Gaia*-Enceladus at high orbital energies, while counter-rotational stars with $V_{\phi} < -200$ km s $^{-1}$ are from the Sequoia.

Additionally, we notice the enhancement of stars with $V_{\phi} = 50 - 200$ km s $^{-1}$ in the region of $Z_{\max} < 5$ kpc of the IHP in Figure 8. This may be due to a metal-weak thick-disk (MWTD) population. Carollo et al. (2010) identify such a population, which they speculate could be kine-

matically independent of the canonical thick disk, with net rotation $V_\phi = 100 - 150 \text{ km s}^{-1}$ within 5 kpc of the Galactic plane using the SDSS DR7, which has characteristics similar to those of the enhancement found in our sample. Additional data from Beers et al. (2014) and Carollo et al. (2019) bolster this interpretation. Another explanation for the enhancement may be in situ stars formed in a protodisk and heated up as described by McCarthy et al. (2012). Using the sample of 412 MW-mass disk galaxies in the Galaxies-Intergalactic Medium Interaction Calculation suite of cosmological hydrodynamical simulations, they show that in situ stars with prograde motions dominate at $r \leq 30$ kpc, whereas the outer halo is dominated by accreted stars. They obtain a median rotational lag of -0.35 (normalized by V_{LSR}) of the in situ component in the stacked sample limited to the solar neighborhood. Adopting $V_{\text{LSR}} = 220 \text{ km s}^{-1}$ for the MW, the median rotational velocity of the in situ stars is $143 (= 220 \times (1 - 0.35)) \text{ km s}^{-1}$, which is in the range we find as well.

Furthermore, our sample of stars suggests that, due to the different orbital characteristics between metal-poor and metal-rich stars, the metal-poor stars are dominant beyond $Z_{\text{max}} = 15$ kpc in the inner halo and above $Z_{\text{max}} = 25$ kpc in the outer halo, when separating the halo regions at $r_{\text{max}} = 30$ kpc. It is also possible to identify the shift of the MDF to be more metal-poor for $r_{\text{max}} > 30$ kpc. As a result, the OHP is more metal-poor than the IHP. These characteristics agree with the features found in the in situ halo sample of red giants by Chen et al. (2014), who report that the transition from the inner to outer halo occurs at a vertical distance $|Z| \sim 20$ kpc from the Galactic plane and at a distance of $r \sim 35$ kpc from the Galactic center. Although the transition regions differ, our findings on the dual nature of the Galactic halo are also supported by the analyses of photometric samples, which suffer less from potential target-selection bias. Those results indicate that the halo out to ~ 10 kpc from the Sun is comprised of two stellar components (An et al. 2013, 2015), and the metallicity of the halo varies between 10 and 20 kpc in Galactocentric distance (de Jong et al. 2010).

7. SUMMARY

We have presented a study of the dependence of derived Galactic halo properties, employing two well-known, frequently used Galactic potentials (the Stäckel and the Galpy), based a local sample of stars selected from the spectrophotometric calibration and telluric standard stars of SDSS DR12, using the criteria of Carollo et al. (2010).

We found that the shape of the MDF and the rotational velocity distribution abruptly change at 15 kpc of Z_{max} in the Stäckel potential, which suggests that the transition from the inner to outer halo occurs at that distance. We further confirmed that the stars in the outer-halo region show a retrograde motion of $V_\phi = -60 \text{ km s}^{-1}$ and a mean metallicity of $[\text{Fe}/\text{H}] = -1.9$. In contrast, when the Galpy potential is used, even though we identified the transition of the metallicity distribution at $Z_{\text{max}} = 25$ kpc, there is no noticeable retrograde motion found. It is interesting to note that the unbound stars under the Galpy potential show retrograde motions regardless of Z_{max} , whereas the bound and unbound stars in the

same Z_{max} bins exhibit different MDFs. At any rate, as these discrepancies arise from the different energies of individual stars, we explored halo properties with r_{max} , which is more correlated with orbital energy.

The exploration of our sample with r_{max} revealed that the MDF and rotational velocity distribution are shifted to more metal-poor and retrograde motions at $r_{\text{max}} = 30$ kpc in the Stäckel potential. According to these results, we have newly defined the OHP as stars with $r_{\text{max}} > 30$ kpc. By this division, we found that the OHP consists of a mixture of metal-rich and metal-poor stars, both of which are found among the stars with retrograde motions. Furthermore, the two stellar components exhibit different kinematic characteristics, depending on Z_{max} , in the sense that the metal-rich stars exhibit large radial motions regardless of Z_{max} , whereas the metal-poor stars have primarily radial motions at lower Z_{max} , but more polar motions at higher Z_{max} . We also found that the profiles of the rotation velocity and metallicity over r_{max} for the OHP exhibit a retrograde motion as low as $V_\phi = -150 \text{ km s}^{-1}$ and metallicity down to $[\text{Fe}/\text{H}] = -1.7$. Conversely, the halo stars under the Galpy potential do not exhibit such a dual nature in either the MDFs or rotational velocity distribution.

The reason for the dissimilar characteristics inferred for halo stars between the Stäckel and the Galpy potential analyses stems from the fact that stars with high retrograde motions in the Stäckel potential are unbound in the Galpy potential, and stars with low rotational velocities reach to more distant Z_{max} and r_{max} , due to the shallower Galpy potential. Because the observed nature of the halo differs, depending on the adopted Galactic potential, it is clear that a more realistic Galactic potential is required going forward, particularly when using only relatively local samples of halo stars.

We thank an anonymous referee for a careful review of this paper, which has improved the clarity of its presentation.

Funding for SDSS-III was provided by the Alfred P. Sloan Foundation, the Participating Institutions, the National Science Foundation, and the U.S. Department of Energy Office of Science. The SDSS-III Web site is <http://www.sdss3.org/>.

Y.S.L. acknowledges support from the National Research Foundation (NRF) of Korea grant funded by the Ministry of Science and ICT (No.2017R1A5A1070354 and NRF-2018R1A2B6003961). T.C.B. acknowledges partial support for this work from grant PHY 14-30152; Physics Frontier Center/JINA Center for the Evolution of the Elements (JINA-CEE), awarded by the U.S. National Science Foundation.

REFERENCES

- Abadi, M. G., Navarro, J. F., & Steinmetz, M. 2006, MNRAS, 365, 747
- Abazajian, K. N., Adelman-McCarthy, J. K., Agüeros, M. A., et al. 2009, ApJS, 182, 543
- Alam, S., Albareti, F. D., Allende Prieto, C., et al. 2015, ApJS, 219, 12
- Allende Prieto, C., Sivarani, T., Beers, T. C., et al. 2008, AJ, 136, 2070
- Allende Prieto, C., Fernandez-Alvar, E., Schlesinger, K. J., et al. 2014, A&A, 568, 7

- An, D., Beers, T. C., Johnson, J. A., et al. 2013, *ApJ*, 763, 65
- An, D., Beers, T. C., Santucci, R. M., et al. 2015, *ApJ*, 813, 28
- Amorisco, N. C. 2017, *MNRAS*, 464, 2882
- Beers, T. C., Chiba, M., Yoshii, Y., et al. 2000, *AJ*, 119, 2866
- Beers, T. C., Carollo, D., Ivezić, Ž., et al. 2012, *ApJ*, 746, 34
- Beers, T. C., Norris, J. E., Placco, V. M., et al. 2014, *ApJ*, 794, 58
- Belokurov, E., Zucker, D. B., Evans, N. W., et al. 2006, *ApJ*, 642, 137
- Belokurov, E., Erkal, D., Evans, N. W., et al. 2018, *MNRAS*, 478, 611
- Bland-Hawthorn, J., & Gerhard, O. 2016, *ARA&A*, 54, 529
- Bonaca, A., Jurić, M., Ivezić, Ž., et al. 2012, *AJ*, 143, 105
- Bonaca, A., Conroy, C., Wetzell, A., et al. 2017, *ApJ*, 845, 101
- Bovy, J. 2015, *ApJS*, 216, 29
- Bullock, J. S., & Johnston, K. V. 2005, *ApJ*, 635, 931
- Carollo, D., Beers, T. C., Lee, Y. S., et al. 2007, *Nature*, 450, 1020
- Carollo, D., Beers, T. C., Chiba, M., et al. 2010, *ApJ*, 712, 692
- Carollo, D., Chiba, M., Ishigaki, M. N., et al. 2019, [arXiv:1904.04881v2](https://arxiv.org/abs/1904.04881v2)
- Chen, Y. Q., Zhao, G., Carrell, K., et al. 2014, *ApJ*, 795, 52
- Chiba, M., & Beers, T. C. 2000, *AJ*, 119, 2843
- Cooper, A., Parry, O. H., Lowing, B., Cole, S., & Frenk, C. 2015, *MNRAS*, 454, 3185
- Cui, X. Q., Zhao, Y. H., Chu, Y. Q., et al. 2012, *RAA*, 12, 1197
- Das, P., & Binney, J. 2016, *MNRAS*, 460, 1725
- Dawson, K. S., Schlegel, D. J., Ahn, C., et al. 2013, *AJ*, 145, 10
- Deason, A. J., Belokurov, V., & Evans, N. W. 2011, *MNRAS*, 411, 1480
- Dejonghe, H., & de Zeeuw, T. 1988, *ApJ*, 333, 90
- de Jong, J. T. A., Yanny, B., Rix, H.-W., et al. 2010, *ApJ*, 714, 663
- de Zeeuw, T., Peletier, R., & Franx, M. 1986, *MNRAS*, 221, 1001
- Fernandez-Alvar, E., Allende Prieto, C., Schlesinger, K. J., et al. 2015, *A&A*, 577, 81
- Font, A. S., McCarthy, I. G., Crain, R. A., et al. 2011, *MNRAS*, 416, 2802
- Gaia Collaboration, Brown, A. G. A., Vallenari, A., et al. 2018, *A&A*, 616, 1
- Helmi, A., Babusiaux, C., Koppelman, H. H., et al. 2018, *Nature*, 563, 85
- Hogg, D. W., Blanton, M. R., Roweis, S. T., & Johnston, K. V. 2005, *ApJ*, 629, 268
- Kafle, P. R., Sharma, S., Lewis, G. F., & Bland-Hawthorn, J. 2013, *MNRAS*, 430, 2973
- Kafle, P. R., Sharma, S., Robotham, A. S. G., et al. 2017, *MNRAS*, 470, 2959
- Kerr, F. J., & Lynden-Bell, D. 1986, *MNRAS*, 221, 1023
- Lee, Y. S., Beers, T. C., Sivarani, T., et al. 2008a, *AJ*, 136, 2022
- Lee, Y. S., Beers, T. C., Sivarani, T., et al. 2008b, *AJ*, 136, 2050
- Lee, Y. S., Beers, T. C., Allende Prieto, C., et al. 2011, *AJ*, 141, 90
- Lindgren, L., Hernández, J., Bombrun, A., et al. 2018, *A&A*, 616, 2
- Majewski, S., Skrutskie, M. F., Weinberg, M. D., et al. 2003, *ApJ*, 509, 1082
- McCarthy, I. G., Font, A. S., Crain, R. A., et al. 2012, *MNRAS*, 420, 2245
- Mints, A., & Hekker, S. 2019, *A&A*, 621, 17
- Munn, J. A., Monet, D. G., Levine, S. E., et al. 2004, *AJ*, 126, 3034
- Munn, J. A., Monet, D. G., Levine, S. E., et al. 2008, *AJ*, 136, 895
- Myeong, G. C., Evans, N. W., Belokurov, E., et al. 2018, *ApJ*, 856, 26
- Myeong, G. C., Vasiliev, E., Iorio, G., et al. 2019, *MNRAS*, 488, 1235
- Newberg, H. J., Yanny, B., Rockosi, C., et al. 2002, *ApJ*, 569, 245
- Quinn, P. J., & Goodman, J. 1986, *ApJ*, 309, 472
- Ruchti, G. R., Read, J. I., Feltzing, S., et al. 2014, *MNRAS*, 444, 515
- Schlegel, D. J., Finkbeiner, D. P., & Davis, M. 1998, *ApJ*, 500, 525
- Schönrich, R., Asplund, M., & Casagrande, L. 2011, *MNRAS*, 415, 3807
- Schönrich, R., Asplund, M., & Casagrande, L. 2014, *ApJ*, 786, 7
- Schönrich, R., McMillan, P., & Eyer, L. 2019, *MNRAS*, 487, 3568
- Smolinski, J. P., Lee, Y. S., Beers, T. C., et al. 2011, *AJ*, 141, 89
- Sommer-Larsen, J., & Zhen, C. 1990, *MNRAS*, 242, 10
- Tian, H., Liu, C., Xu, Y., et al. 2019, *ApJ*, 871, 184
- Tissera, P. B., White, S. D. M., & Scannapieco, C. 2012, *MNRAS*, 420, 255
- Tissera, P. B., Scannapieco, C., Beers, T. C., & Carollo, D., 2013, *MNRAS*, 432, 3391
- Tissera, P. B., Beers, T. C., Carollo, D., & Scannapieco, C. 2014, *MNRAS*, 439, 3128
- Tissera, P. B., Machado, R. E. G., Carollo, D., et al. 2018, *MNRAS*, 473, 1656
- Van den Bosch, F. C., Lewis, G. F., Lake, G., & Stadel, J. 1999, *ApJ*, 515, 50
- Venn, K. A., Irwin, M., Shetrone, M. D., et al. 2004, *AJ*, 128, 1177
- White, S. D. M., & Frenk, C. S. 1991, *ApJ*, 379, 52
- Yanny, B., Newberg, H. J., Kent, S., et al. 2000, *ApJ*, 540, 825
- Yanny, B., Newberg, H. J., Johnson, J. A., et al. 2009, *AJ*, 137, 4377
- York, D. G., Adelman, J., Anderson, J. E., Jr., et al. 2000, *AJ*, 120, 1579
- Zolotov, A., Willman, B., Brooks, A. M., et al. 2009, *ApJ*, 702, 1058